

Review

Airborne spectral BRDF of various surface types (ocean, vegetation, snow, desert, wetlands, cloud decks, smoke layers) for remote sensing applications

Charles K. Gatebe ^{a,b,*}, Michael D. King ^c^a Universities Space Research Association (USRA), Columbia, MD, USA^b NASA Goddard Space Flight Center, Greenbelt, MD, USA^c Laboratory for Atmospheric and Space Physics, University of Colorado, Boulder, CO, USA

ARTICLE INFO

Article history:

Received 29 September 2015

Received in revised form 18 March 2016

Accepted 23 March 2016

Available online 6 April 2016

Keywords:

BRDF
Albedo
Directional reflectance
Remote sensing
Airborne
Ocean
Vegetation
Savannah
Croplands
Snow
Sea ice
Desert
Wetlands
Clouds
Smoke layers

ABSTRACT

In this paper we describe measurements of the bidirectional reflectance-distribution function (BRDF) acquired over a 30-year period (1984–2014) by the National Aeronautics and Space Administration's (NASA's) Cloud Absorption Radiometer (CAR). Our BRDF database encompasses various natural surfaces that are representative of many land cover or ecosystem types found throughout the world. CAR's unique measurement geometry allows a comparison of measurements acquired from different satellite instruments with various geometrical configurations, none of which are capable of obtaining such a complete and nearly instantaneous BRDF. This database is therefore of great value in validating many satellite sensors and assessing corrections of reflectances for angular effects. These data can also be used to evaluate the ability of analytical models to reproduce the observed directional signatures, to develop BRDF models that are suitable for sub-kilometer-scale satellite observations over both homogeneous and heterogeneous landscape types, and to test future spaceborne sensors. All of these BRDF data are publicly available and accessible in hierarchical data format (<http://car.gsfc.nasa.gov/>).

© 2016 Elsevier Inc. All rights reserved.

Contents

1. Introduction	132
2. BRDF terminology and CAR BRDF data	132
3. The CAR instrument	134
4. Optical characteristics of BRDF	135
4.1. Oceans and lakes	137
4.2. Vegetated surfaces (forests, savannas, croplands)	137
4.3. Clouds (liquid water and ice)	140
4.4. Snow and sea ice	140
4.5. Non-vegetated bright surfaces (dry lakebeds, desert)	142
4.6. Wetlands	143
4.7. Smoke (biomass and oil)	147
5. Summary and conclusions	147

* Corresponding author.

E-mail address: charles.k.gatebe@nasa.gov (C.K. Gatebe).

Acknowledgments	147
References	147

1. Introduction

In this paper, we describe measurements of bidirectional reflectance-distribution function (BRDF) acquired over a 30-year period (1984–2014) by the National Aeronautics and Space Administration's (NASA's) Cloud Absorption Radiometer (CAR). These multidirectional measurements provide a unique remote sensing perspective on different surfaces such as ocean, vegetation, snow, desert, wetlands, cloud decks, and smoke layers. These data may be used to evaluate the ability of analytical models to reproduce observed directional signatures and to develop BRDF models that are suitable for sub-kilometer-scale satellite observations over both homogeneous and heterogeneous landscape types.

BRDF observations are now becoming increasingly important when dealing with higher spatial resolution satellite products over heterogeneous landscapes in accounting for view-illumination angular effects caused by surface inhomogeneity. This is demonstrated by Longbotham et al. (2012), who assessed the value of high-resolution multiangle data by comparing the performance of urban multiangle classification experiments to the classification performance of a single WorldView-2 multispectral image. The study showed that there is significant improvement in classification accuracy available from leveraging the spatial and spectral data in a multiangle WorldView-2 image sequence, as well as provided the ability to differentiate classes that are generally difficult to distinguish, such as skyscrapers, bridges, high-volume highways, and parked cars. In a similar study, Koukal and Atzberger (2012) demonstrated that multiangular data permits a better discrimination of five forest types as compared to the sole use of spectral information. Other application areas described in the literature (cf. Diner et al. (1999, 2005)) include cloud radiative forcing, where directional measurements are needed in the derivation of cloud albedo, cloud type, and characterization of cloud morphologies and also aerosol climatic effects, where oblique views provide increased optical path length through the atmosphere and wider range of scattering angles that could enable aerosol types of varying compositions and sizes to be distinguished. A more in-depth review of multiangular measurements appears in the International Forum on BRDF special issue on application of multiangular remote sensing in the study of the earth's land, ocean and atmosphere (Liang & Strahler, 2000). In planetary studies, multiangular measurements are needed for correctly interpreting radiation reflected from a given area of the surface at a given time, or a given illumination and viewing geometry.

Current satellite systems are capable of measuring reflected energy, but in limited directions. Satellites that provide near-simultaneous multi-angle measurements include the Multi-angle Imaging Spectro-Radiometer (MISR) on NASA's Terra satellite, which obtains spectral radiance images from nine different directions (0° , $\pm 26.1^\circ$, $\pm 45.6^\circ$, $\pm 60.0^\circ$ and $\pm 70.5^\circ$) in the along-track direction over a period of 7 min (Diner, Di Girolamo, & Nolin, 2007; Diner et al., 1998). The Compact High Resolution Imaging Spectrometer (CHRIS) on the European Space Agency's (ESA's) Program for On-Board Autonomy (PROBA) satellite provides spectral radiance images at five angles (0° , $\pm 36^\circ$, and $\pm 55^\circ$) in the along-track direction over a period of 3 min in a narrow swath width of 14 km (Barnsley, Settle, Cutter, Lobb, & Teston, 2004). The Japanese launched the first of their ADEOS (Advanced Earth Observing Satellite) satellites in 1996. It contained the POLDER (Polarization of the Earth's Reflectances) instrument, a polarization-sensitive charge-coupled device (CCD) camera from the Centre National d'Etudes Spatiales (CNES), which views a surface target in 12 directions (along-track and cross-track FOVs (fields of view) of $\pm 43^\circ$ and $\pm 51^\circ$) and a wide range of azimuth angles, with a spatial resolution of about 6 km (Deschamps et al., 1994; Hautecoeur and Leroy (1998); Tanré et al., 2011). It subsequently flew on both ADEOS 2 and the CNES PARASOL

(Polarization and Anisotropy of Reflectances for Atmospheric Sciences coupled with Observations from a Lidar) satellites. Other satellite instruments, such as AVHRR (Advanced Very High Resolution Radiometer), MODIS (Moderate-resolution Imaging Spectroradiometer), and VEGETATION, accumulate directional data on subsequent orbits. For example, NASA's MODIS samples the BRDF by virtue of its across-track sampling and multi-angle datasets are accumulated over the course of up to 16 days for the standard product (Schaaf et al., 2002).

The CAR (Fig. 1), an airborne instrument first developed for measuring scattered solar radiation deep within cloud layers for the purpose of deriving the spectral single scattering albedo, or absorption, of a cloud layer (King, Radke, & Hobbs, 1990; King, Strange, Leone, & Blaine, 1986), has for decades been used for measuring the angular distribution of reflected solar radiation of natural ecosystems worldwide. These measurements can be used to derive the complete spectral BRDF at the full range of zenith and azimuth angles, and thus are valuable for assessing the accuracy of satellite-derived BRDFs (cf. Abdou et al. (2006); Román et al. (2011)).

The intent of this paper is to summarize the wide variety of BRDFs that have been obtained from 1991 to the present, where the measurements have been acquired from six different aircraft and over four different continents (Asia, Africa, North America and South America). The various ecosystems and environmental conditions that have been observed include: (i) water bodies (oceans and lakes), (ii) vegetation (savanna, cropland, forest), (iii) clouds (liquid water, ice, and supercooled), (iv) snow and sea ice, (v) bright, nonvegetated surfaces (salt pans, desert), (vi) wetlands (mangroves and swamps), and (vii) smoke from forest fires.

2. BRDF terminology and CAR BRDF data

In order to understand the reflectance characteristics of different surfaces of a semi-infinite particle medium, we can use the physical optics approach, which uses electromagnetic wave theory to analyze the directional scattering properties of the surface, but it presents great theoretical challenges due to the large degrees of freedom involved and needs to include multiple scattering effects (cf. Hapke (1981)). The geometrical optics approach, which is mathematically simpler, makes use of the ray-like nature of light to explain the gross behavior of light when the wavelength is small compared with the pertinent physical dimensions of the system (Torrence & Sparrow, 1967). The geometrical approach is used in some physics textbooks to define "reflectance" as the ratio of the amount of light reflected from a surface to the amount of incident light (e.g. Lenoble, 1993; Rees, 1990), where the ratio of the amount of light reflected from a surface to the amount of light reflected from a standard diffuse white surface is defined as "reflectance factor." The two should not be confused as they represent different physical quantities and can have different numerical values for the same measured target (McCamy, 2001). However, according to the U.S. National Institute of Standards and Technology (NIST), the basic parameter for describing (geometrically) the reflecting properties of a surface element is the BRDF; (Nicodemus, Richmond, Hsia, Ginsberg, & Limperis, 1977). The mathematical form used to describe the spectral BRDF, f_r , can be expressed in the form:

$$f_r(\theta_i, \varphi_i; \theta_r, \varphi_r) = \frac{dL_r(\theta_i, \varphi_i; \theta_r, \varphi_r; E_i)}{dE_i(\theta_i, \varphi_i)} \quad (1)$$

where $dL_r(\theta_i, \varphi_i; \theta_r, \varphi_r; E_i)$ is the reflected radiance in some outgoing direction (θ_r, φ_r) , and $dE_i(\theta_i, \varphi_i)$ is the elemental incident irradiance

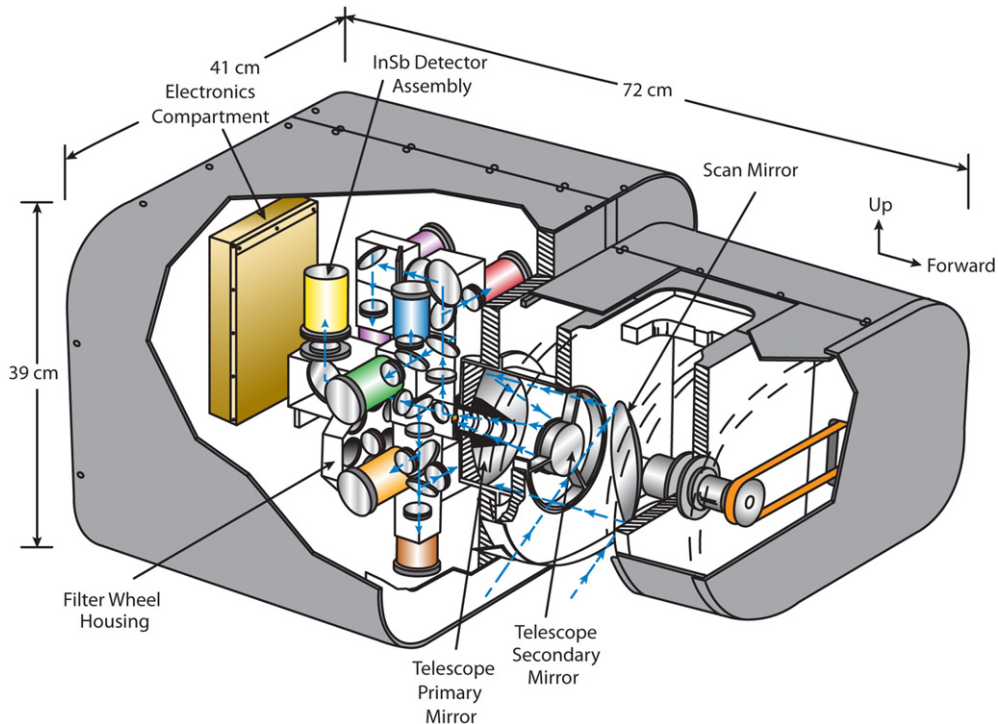


Fig. 1. Cutaway drawing of the CAR. The instrument housing is approximately 72 cm long, 41 cm wide, and 39 cm deep and weighs 42 kg. The CAR has 14 narrow spectral bands between 0.34 and 2.30 μm . The CAR images the sky and surface at an instantaneous field of view (IFOV) of $\sim 1^\circ$ through any plane defined by 190° .

from a source in some incoming direction (θ_i, φ_i). The polar angles ($\theta_i; \theta_r$) are measured from the surface normal and the azimuth angles ($\varphi_i; \varphi_r$) are measured from any arbitrary reference in the surface plane containing the incident beam. The subscript “r” in Eq. (1) denotes that the BRDF is evaluated at a point on a flat plane surface that is assumed to have uniform and isotropic scattering properties (Nicodemus et al., 1977). With this definition, f_r has the units of sr^{-1} and according to Nicodemus (1970), BRDF may have extremely high values, even going to infinity in the delta function form for ideally specular reflectance. Considering that BRDF is a ratio of two infinitesimally small quantities, it can never be measured directly because truly infinitesimal elements of solid angle do not include measurable amounts of radiant flux. To get measurable optical properties, we assume that the effective BRDF (f_e^e) at a horizontal reference plane is an average over an appropriate area, angle and solid angle, for a particular source-target-sensor geometry given by:

$$f_e^e(\theta_i, \varphi_i; \theta_r, \varphi_r) = \frac{\Delta L_r(\theta_i, \varphi_i; \theta_r, \varphi_r; E_i)}{\Delta E_i(\theta_i, \varphi_i)} = \frac{\Delta L_r(\theta_i, \varphi_i; \theta_r, \varphi_r; E_i)}{\Delta L_i(\theta_i, \varphi_i) \cos \theta_i \Delta \omega_i} \quad (2)$$

where $\Delta E_i(\theta_i, \varphi_i) = \Delta L_i(\theta_i, \varphi_i) \cos \theta_i \Delta \omega_i$, $\Delta \omega_i$ is a finite solid angle element within which the incident radiance (L_i) is confined in the direction (θ_i, φ_i). For most applications, the validity of this approximation is based on experimental evidence that BRDF is not significantly influenced by the effects of finite intervals of area, angle, solid angle, and distribution function; effects of sub-surface scattering; effects of other radiation parameters such as wavelength and polarization and of fluorescence, or phosphorescence (Nicodemus et al., 1977).

Since BRDF is a fundamental quantity describing optical scattering from a surface, other reflectance quantities such as the bidirectional reflectance factor (BRF), hemispherical-directional reflectance factor (HDRF), directional-hemispherical reflectance (DHR), hemispherical-directional reflectance factor (HDRF), and bihemispherical reflectance (BHR or albedo) can be expressed in terms of f_r (cf. Hapke (1981); Martonchik et al. (2000); Schaepman-Strubet et al. (2006)). The Earth remote sensing community has adopted this NIST nomenclature as it

provides a good theoretical basis for understanding and relating physical measurements in one situation to another.

In this paper, following the same NIST nomenclature, CAR data are defined by Eq. (3):

$$f_r^e(\theta_0, \theta, \varphi) = \frac{L_r^e(\theta_0, \theta, \varphi)}{F_{0,\lambda}(\theta_0) \cos \theta_0} \quad (3)$$

where f_r^e is the effective BRDF, L_r^e is the actual measured radiance in any given direction, $F_{0,\lambda}$ is the solar irradiance incident on the top of the atmosphere, assuming mean Sun-Earth distance, θ_0 and θ , are the incident and viewing incident zenith angles, respectively, and φ is the relative azimuth angle between the viewing and incident light directions. For direct comparison with measurements from other similar sensors, CAR data can be converted to an equivalent BRF, a non-dimensional quantity equivalent to effective BRDF times $\pi (\pi f_r^e)$, which shows quickly the difference between the measured surface and a Lambertian reflector.

CAR data are stored and distributed as Hierarchical Data Format (HDF), which is the standard data storage format selected by the NASA Earth Observing System Data and Information System (EOSDIS). Each HDF data file contains calibrated Earth and/or sky view observations for CAR bands index 1–8, where the 8th band index is selected among the filter wheel bands (see Table 1, bands 8–13). Files are identified by field mission and flight number, where each flight is defined by aircraft takeoff to aircraft landing (see Table 2). For each CAR band, BRDF data are formatted in a polar coordinate system, where the view directions range from 0 to 180° in half-degree intervals, and the relative azimuth angles range from 0 to 360° , in one degree intervals. Thus, an azimuth of 0° (or 360°) and 180° represents forward scattering and backscattering, respectively. The contribution of the skylight on the viewed surface within the instrument IFOV is assumed to be small, especially for clear sky measurements with low aerosol optical depth.

Note that various radiative transfer schemes have been used for the atmospheric correction of these BRDF measurements (cf. Gatebe et al. (2005); Gatebe et al. (2003)). We can remove the effects of atmospheric absorption and scattering from our BRDF measurements as demonstrated

Table 1
CAR band configurations/30-year period.

Band index	Central wavelength [bandpass] nm			
	1984–1993	1994–1998	1999–2011	2014
1	502 [16]	472 [21]	472 [21]	480 [21]
2	673 [20]	675 [20]	682 [22]	687 [26]
3	754 [19]	300 [?]	340 [9]	340 [9]
			381 [6]	381 [6]
4	866 [20]	868 [20]	870 [20]	870 [10]
5	1031 [20]	1038 [20]	1036 [22]	1028 [4]
6	1220 [22]	1271 [22]	1219 [22]	609 [9]
7	1270 [21]	1219 [21]	1273 [23]	1275 [24]
8	1547 [30]	1552 [30]	1556 [32]	1554 [33]
9	1640 [41]	1643 [41]	1656 [45]	1644 [46]
10	1722 [38]	1725 [38]	1737 [40]	1713 [46]
11	2100 [39]	2100 [39]	2103 [44]	2116 [43]
12	2200 [40]	2207 [40]	2205 [42]	2203 [43]
13	2289 [23]	2302 [23]	2302 [43]	2324 [48]

in Fig. 4a, b, & c using the second simulation of satellite signal in the solar spectrum (6S) model (Gatebe et al., 2003; Vermote, Tanré, Deuzé, Herman, & Morcrette, 1997). For the ocean cases (e.g. as shown in Fig. 4d), we can use a method of spherical harmonics with Cox and Munk (1954a, 1954b) wave-slope distribution to solve the atmosphere-ocean radiation transport problem as described in Gatebe et al. (2005). In all cases, CAR data product contains BRDF, but the plotted values have been converted to equivalent BRF values to help differentiate between the reflectance of the measured surface and a Lambertian reflector.

3. The CAR instrument

The CAR (Fig. 1) is an airborne multiwavelength scanning radiometer that was originally designed and built in 1983 as a 13-channel scanning radiometer (King et al., 1986), and subsequently upgraded to a 14-channel radiometer in 2000 (Gatebe et al., 2003). The instrument is non-dispersive, being composed of a complex configuration of beam splitters and narrowband interference filters. Table 1 shows how the band center and bandwidth characteristics have evolved over a 30-year operational period from 1984 to 2014. The instrument was designed to operate from a position mounted on various aircraft platforms (cf.

Fig. 2). It has a novel design with a wide field of regard (190°) and a small instantaneous field of view (1°), which allows it to scan in a plane perpendicular to the direction of flight. A self-contained navigation system for the CAR, known as the CANS (CAR Autonomous Navigation System), includes a GPS (Global Positioning System), roll axis inertia and rates, and three axis acceleration, thereby providing roll correction to the sensor with respect to aircraft roll in real time, based upon inputs from a precision navigation sensor. CANS is integrated into the CAR support structure and data system (Kahle, Gatebe, McCune, & Dustan, 2013).

In the normal mode of operation onboard an aircraft, the CAR views 190° of the Earth-atmosphere scene around the starboard horizon. This configuration permits observations of both local zenith and nadir, provided the aircraft roll is $<5^\circ$ and pitch is $<1^\circ$. In addition to the starboard viewing mode, the CAR instrument can be rotated in-flight into any viewing positions, e.g., downward-looking imaging mode, where the CAR views 190° of the Earth scene from horizon to horizon and upward-looking imaging mode, where the CAR views 190° of the sky above the aircraft from horizon to horizon. Data are always sampled simultaneously and continuously for spectral bands 0.34 to $1.27\text{ }\mu\text{m}$, plus one of the six bands on the filter wheel (1.55 – $2.30\text{ }\mu\text{m}$). The filter wheel can either cycle through all six spectral bands at a prescribed interval (usually changing filter every fifth scan line), or lock onto any one of the six spectral bands, usually 1.66 , 2.10 , or $2.21\text{ }\mu\text{m}$, and sample it continuously. Calibration of the CAR is performed in-house at Goddard Space Flight Center (GSFC) prior to and just after a field deployment (Gatebe, Butler, Cooper, Kowalewski, & King, 2007).

To measure the BRDF of a surface, the plane can bank at any angle, but typically banks at a comfortable roll angle of $\sim 20^\circ$ and flies a circle about 3 km in diameter above the surface, often repeating several orbits over a uniform ecosystem. The unique instrument design, coupled with the lateral mobility of the aircraft in a circular flight track, enables a nearly complete coverage of the zenith and azimuth angles of a full-hemisphere of BRDF measurements in a relatively short time of ~ 2 – 3 min. The aircraft platform provides added benefits of being able to fly above any surface at different heights to acquire measurements at varying spatial resolutions or grid sizes. For example, from an altitude of 1000 m, the pixel resolution is about 18 m at nadir and about 580 m at 80° viewing angle. The CAR collects between 76,400 and 114,600 directional measurements of radiance per channel per

Table 2
CAR field campaigns (1984–2014).

Experiment	Location	Dates	Flight number	Flight hours
Check Flights	Washington State	Jan 12, 1984–July 22, 1986	1136–1264	18
FIRE	San Diego, California	June 29–July 16, 1987	1296–1308	30
Alaska 90	Alaska (Beaufort Sea, Barrow, Deadhorse)	June 13–24, 1990	1445–1455	>18
Kuwait Oil Fire 91	Kuwait Oil Fires	May 16–June 3, 1991	1477–1486	>30
LeadEx	Deadhorse, Alaska	April 7–19, 1992	1539–1546	33
ASTEX	Azores, Portugal	June 2–23, 1992	1557–1570	46
SCAR-A	US East Coast (Great Dismal Swamp, Hog Island, Pine Barrens)	July 12–28, 1993	1605–1612	>21
MAST	Monterey, California	June 1–30, 1994	1638–1649	>19
ARMCAS	Alaska (Deadhorse)	June 3–14, 1995	1675–1684	>29
SCAR-B	Brazil (Brasilia, Cuiaba, Mato Grosso, Porto Velho, Rondonia)	August 17–September 11, 1995	1688–1704	22
TARFOX	Wallop Island	July 20, 1996	1722–1737	>46
FIRE ACE	Alaska (Barrow)	May 20–June 24, 1998	1751–1772	>82
SAFARI 2000	South Africa, Zambia, Namibia, Botswana	August 15–September 16, 2000	1814–1839	100
CLAMS	Atlantic Ocean off US East Coast	July 10–August 2, 2001	1870–1882	34
Skukuza	South Africa	June 18–20, 2005	1900–1903	7
INTEX-B/ MILAGRO	Mexico (Gulf of Mexico, Mexico City)	March 3–20, 2006	1905–1918	43
CLASIC	Oklahoma, USA	June 13–25, 2007	1919–1929	20
ARCTAS	US (Alaska, California), Canada, Greenland	April 6–July 12, 2008	2001–2023	>138
ECO-3D	US (Maine, Massachusetts, Florida, New Hampshire)	August 19–September 19, 2011	2024–2036	>67
DISCOVER-AQ	Colorado	July 8–August 12, 2014	2037–2061	>98

Acronyms (used in Table 2): FIRE: the First ISCCP (International Satellite Cloud Climatology Project) Regional Experiment; LeadEx: Arctic Lead Experiment; ASTEX: Atlantic Stratocumulus Transition Experiment; SCAR-A: Smoke/Sulfates, Clouds and Radiation – America; MAST: Monterey Area Ship Tracks; ARMCAS: Arctic Radiation Measurement in Column: Atmosphere-surface System; SCAR-B: Smoke/Sulfates, Clouds and Radiation – Brazil; TARFOX: Tropospheric Aerosol Radiative Forcing Observational Experiment; FIRE ACE: FIRE Arctic Cloud Experiment; SAFARI-2000: Southern African Regional Science Initiative-2000; CLAMS: Chesapeake Lighthouse and Aircraft Measurements for Satellites; INTEX-B: Intercontinental Chemical Transport Experiment–Phase B; MILAGRO: Megacity Initiative: Local and Global Research Observations; CLASIC: Cloud and Land Surface Interaction Campaign; ARCTAS: Arctic Research of the Composition of the Troposphere from Aircraft and Satellites; DISCOVER-AQ: Deriving Information on Surface Conditions from Column and Vertically Resolved Observations Relevant to Air Quality.



Fig. 2. The CAR has been integrated and flown on six different aircraft from 1984–2014: University of Washington's aircraft (Douglas B-23: 1983–1984, C-131A: 1985–1997 and Convair CV-580: 1998–2001), South African Weather Service Aerocommander 690A (wing mount, June 2005), Sky Research Inc. Jetstream 31 (nose mount, February 2006–June 2007) and NASA's P-3B (2008–).

complete coverage in zenith and azimuthal angles. This amounts to between 687,600 and 1,031,400 directional images per orbit for the nine channels. Final geometric correction is applied by applying pixel offsets along each scan line based on the aircraft roll and pitch data, and ensuring that the pixel corresponding to the horizon is easily identified on a scan line by the contrast between the sky and surface. A plot of sky radiance as a function of azimuthal angle, i.e., observations made in a sweep across the solar disk at a constant elevation angle through 360° of azimuth is used to confirm the symmetry of the sky radiances about the solar principal plane due to errors in the geometrical correction.

We believe using the CAR in this manner is the most mobile and efficient way of measuring a complete surface BRDF, and offers the best tradeoffs with regard to mobility, variation in illumination through a shorter measurement cycle, minimization of self-shading, and adaptability to a wide variety of field conditions. One caveat with this approach is that it is impossible to observe exactly the same patch of ground from all angles from the same altitude. However, this can be overcome by flying the aircraft at different heights, but the target is viewed at varying spatial resolutions. This technique works well for homogenous and planar surfaces both at the scale of the instrument IFOV and field of regard.

As shown in [Table 2](#) and [Fig. 3](#), the CAR has been deployed on a regular basis in field campaigns around the world including deployments to Alaska, Brazil, Canada, Kuwait, Saudi Arabia, Mexico, Portugal (Azores), various places in the continental U.S., and several countries in southern

Africa (Botswana, Namibia, Mozambique, South Africa, and Zambia). It has accumulated over 800 h of science data.

Previous studies based on these CAR field deployments include measurements of smoke layers from the Kuwait oil fires ([King, 1992](#)), cerrado, dense forest, and smoke from forest fires in Brazil ([Tsay, King, Arnold, & Li, 1998](#)), smoke from fires in Canada ([Gatebe, Varnai, Poudyal, Ichoku, & King, 2012](#)), the Saudi Arabian desert, forested wetland, and ocean water containing sunglint over the Atlantic Ocean ([Soulen, King, Tsay, Arnold, & Li, 2000](#); [Gatebe et al., 2005](#); [Gatebe, Dubovik, King, & Sinyuk, 2010](#); [Lin et al., 2016](#)), ship wakes over the Pacific ocean ([Gatebe, Wilcox, Poudyal, & Wang, 2011](#)), and the Persian Gulf ([Soulen et al., 2000](#)). Common arctic surfaces (e.g., snow-covered sea ice, melt-season ice, snow-covered tundra, and tundra shortly after snowmelt) have been reported in [Arnoldet al. \(2002\)](#) and [Lyapustin et al. \(2010\)](#). Measurements of various surfaces throughout southern Africa, including savannas, salt pans, and marine stratocumulus clouds off the coast of Namibia are described in [Gatebe et al. \(2003\)](#). CAR BRDF data from various field deployments were instrumental in an observing system simulation experiment (OSSE) to evaluate a small satellite concept and select an optimal formation architecture that minimizes BRDF uncertainties ([Nag, Gatebe, & Weck, 2015](#)).

4. Optical characteristics of BRDF

Comparison of BRDF patterns is facilitated by converting to BRF, a non-dimensional quantity equivalent to BRDF times π . [Fig. 4](#) shows a

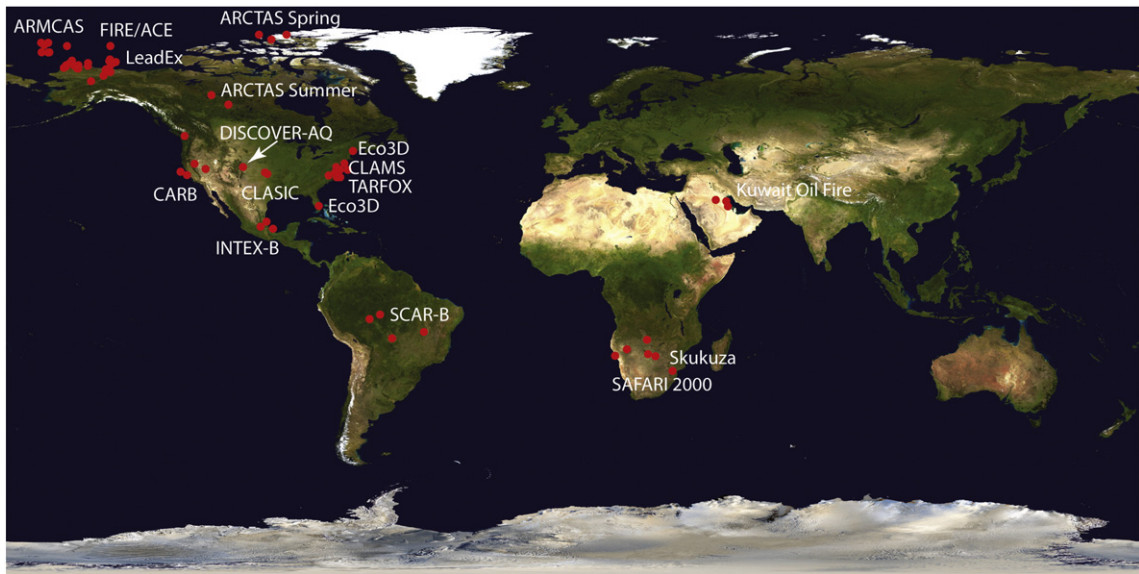


Fig. 3. Locations of airborne measurements of BRDF from different field campaigns from 1987 to 2014 (cf. Table 2). These locations are mainly in the western hemisphere, southern Africa, and Brazil, over different surface types.

composite representation of the BRF as a function of reflected zenith (θ) and azimuth (ϕ) angle, where the distance from the center of the circle (radius) corresponds to the viewing zenith angle (0° – 80°) and the polar

angle is the viewing azimuth angle relative to the sun direction (0° – 360°). The forward scattering direction corresponds to an azimuth of 0° , while the backscattering direction corresponds to an azimuth of

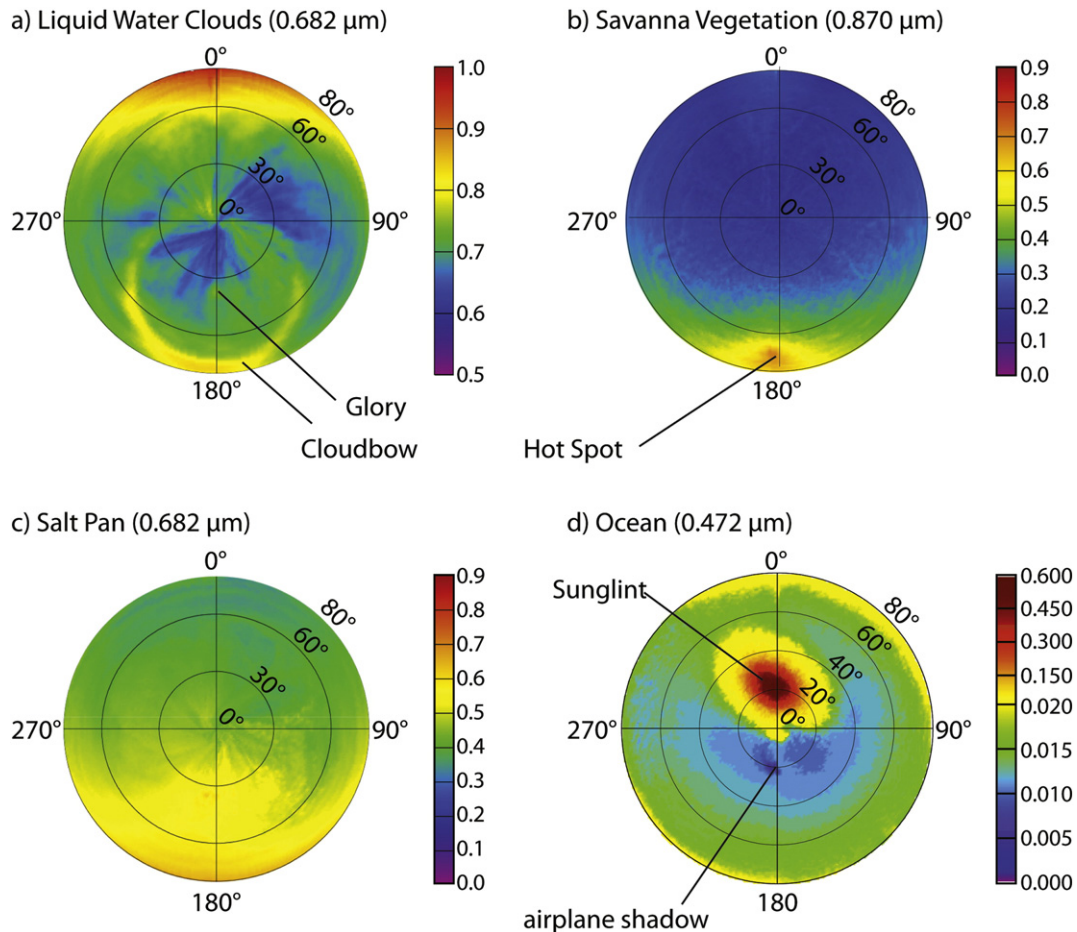


Fig. 4. Images of the BRF at selected wavelengths of the CAR obtained over (a) marine stratocumulus clouds off the Skeleton coast of Namibia (20.5°S , 13.1°E) in late winter (13 September 2000), b) savanna vegetation near Skukuza, South Africa (25.03°S , 31.51°E) on 29 August 2000, (c) Etosha Pan (salt pan) in northern Namibia (19.0°S , 16.0°E) on 16 September 2000, and (d) the Atlantic Ocean in the vicinity of Chesapeake Light (36.91°N , 75.71°W) on 10 July 2001.

180°. The color of the polar diagram shows the magnitude of the measured BRF from nadir to nearly the horizon and for the full range of azimuth angles.

Because of its unique sampling geometry, CAR is able to capture elements of the surface BRDF that are simply not accessible from other scanning instruments at scales that are relevant to satellite remote sensing and encompassing landscapes that are not necessarily homogeneous. Fig. 4 demonstrates this point where the BRF patterns of four surface types (liquid water clouds, savanna vegetation, salt pan, and ocean) show distinct BRF patterns. Fig. 4a shows the BRF at 0.682 μm obtained over marine stratocumulus clouds off the coast of Namibia on 13 September 2000 when the solar zenith angle $\theta_0 = 34^\circ$. These clouds exhibit a distinctive cloudbow at $\sim 42^\circ$ from the antisolar direction and a glory in the antisolar direction, as expected for nearly plane-parallel liquid water clouds. Fig. 4b shows the BRF of savanna vegetation near Skukuza, South Africa (Kruger National Park) obtained at 0.87 μm on 29 August 2000 when $\theta_0 = 67^\circ$. The most distinctive feature of this vegetated surface is its distinct enhancement of reflection in the antisolar direction, known as the hotspot. During SAFARI 2000, observations of the BRDF were also made over several ‘white’ and quite extensive salt pans. Fig. 4c shows the BRF at 0.682 μm obtained over Etosha Pan in northern Namibia on 16 September 2000 when $\theta_0 = 33^\circ$, where the salt pan exhibits a quite uniform reflectance but with enhanced reflectance in much of the backward hemisphere. This was verified by measuring the BRF in the laboratory at Goddard Space Flight Center from Etosha pan samples acquired in Namibia (Georgiev, Gatebe, Butler, & King, 2009). Finally, Fig. 4d shows the BRF of the ocean at 0.472 μm acquired in the vicinity of Chesapeake Light on 10 July 2001, when $\theta_0 = 20^\circ$. The most prominent feature of ocean reflectance is the sunglint in the forward scattering direction, which has a shape and amplitude that is influenced by both wind speed and direction, as discussed in Gatebe et al. (2005). Due to the large dynamic range of the BRF of ocean surfaces from mostly very dark and low reflectance to enhanced reflectance in the sunglint region, the scale for Fig. 4d is bilinear to cover this wide dynamic range. If the computed reflectance for a particular measurement geometry is less than 0.01, we assume the measured BRF value to be in the diffuse radiative regime and plotted in the lower end of the color scale. If the computed reflectance for a particular measurement geometry is greater than 0.01, we assume the measured BRF value to be in the sunglint pattern and plotted in the upper end of the color scale.

Based on broad directional optical features, BRDF of different natural surfaces can be grouped into seven types: (i) water (oceans and lakes), (ii) vegetated surfaces (forests, savanna, croplands, etc.), (iii) clouds (liquid water and ice), (iv) snow and sea ice, (v) non-vegetated surfaces (dry lake beds, desert, and urban-scape), (vi) wetlands (coastal and inland swamps), and (vii) smoke (biomass burning and fuel). The additional surface types from those shown in Fig. 4 include snow and sea ice, whose BRF pattern is similar to the salt pan, but the reflectance is enhanced in the forward scattering direction instead. On the other hand, wetlands combine characteristics of both vegetation and ocean. Smoke from biomass burning or oil burning can fit into the cloud category, but has very unique optical and microphysical characteristics in the shorter wavelengths and is almost transparent in the near-infrared wavelengths. We also recognize that under each category there can be other unique sub-categories. For example, under clouds, we have both liquid water clouds (characterized by having a cloudbow and glory) and ice clouds (characterized by a glint in the forward scattering direction). Each of these subcategories shows a unique view of BRDF anisotropy, or departure from a Lambertian surface.

In the following subsections, we will describe the directional reflectance patterns acquired with the CAR under each of these seven categories using measurements taken at the aircraft flight level. These measurements can be converted conveniently to values at either the surface (with no atmospheric effects) such as in Fig. 4, or at the top of

the atmosphere (with full effects of the atmosphere) using any radiative transfer schemes that would account for all orders of scattering and surface-atmosphere coupling (e.g. Gatebe et al., 2005, 2003; Román et al., 2011).

4.1. Oceans and lakes

Large water bodies such as oceans and lakes have a unique BRDF or BRF pattern, whose appearance is defined by a sun glitter and reflection of the solar aureole, collectively referred to as sunglint (cf. Fig. 5). A calm water body is the only planetary surface, generally speaking, where reflected sunlight approaches the behavior of a mirror surface. However, in nature we find large water bodies show anisotropy of the radiance field just above the water surface outside the glint, which has practical consequences for the interpretation of the water signal detected remotely either by aircraft or satellite-borne radiometers and affects retrieved products such as ocean color and aerosols. The sky radiance that is directly reflected at the air/water interface is highly dependent on the viewing geometry, illumination conditions and sea state (Lin, Li, Gatebe, Poudyal, & Stamnes, 2015). Therefore, ocean color remote sensing requires accurate determination of the contributions of the water leaving radiance and surface reflection effects to above-water radiance signal measured at the sensor level. According to Doxaran, Nagur-Cherukuru, and Lavender (2004), the contribution of surface reflection effects to above-water upwelling radiance measurements is highly variable and always significant (50% in the visible and higher at short and near-infrared wavelengths). It is higher under diffuse light conditions.

Our database includes extensive ocean BRDF measurements over the Atlantic Ocean, especially off the eastern seaboard of the United States in the vicinity of the Chesapeake Light and nearby National Oceanic and Atmospheric Administration (NOAA) buoy stations as described by Gatebe et al. (2005, Table 3). Other ocean cases include measurements over the Pacific Ocean off the western seaboard of the US close to San Francisco, the Atlantic Ocean off the Namibian coastline of Africa, and measurements over the Gulf of Mexico and Persian Gulf. We also have BRDF measurements over other large water bodies such as Lake Tahoe, a large freshwater lake located along the border between California and Nevada, and the Great Slave Lake, the second-largest lake in the Northwest Territories of Canada (480,000 m long) and the deepest lake in North America (614 m). These datasets can be used to evaluate the ability of models to reproduce the observed directional signatures as demonstrated by Lin et al. (2016). The correction of surface reflection effects from water bodies can be problematic because the percentage of sky radiance reflected at the air/water interface is unknown most of the time.

Fig. 5a shows a multispectral image of CAR bands at 1.04, 0.87, and 0.47 μm for reflectance from the ocean in the vicinity of Chesapeake Light on 10 July 2001, when $\theta_0 = 20^\circ$, and Fig. 5b shows a multispectral image for reflectance of Lake Tahoe on 24 June 2008, when $\theta_0 = 41^\circ$. The BRF of each of these observations at 0.47 μm are shown, where the polar plots extend to a zenith angle $\theta = 90^\circ$. The sunglint is readily apparent in the forward scattering portion of each of these polar images, and are clearly illustrated in the corresponding principal plane plots shown in each figure. Note that the BRF scale for the polar plots is adjusted to more clearly illustrate the limb brightening that occurs for $\theta > 80^\circ$, and the sunglint region is saturated in this illustration. Quantitative values are more clearly seen in the principal plane plots. The wind speed over the Atlantic Ocean was $\sim 2 \text{ m s}^{-1}$ (Gatebe et al., 2005), and over Lake Tahoe $\sim 1.8 \text{ m s}^{-1}$, based on wind measurements in the lake by NASA Jet Propulsion Laboratory weather buoy.

4.2. Vegetated surfaces (forests, savannas, croplands)

Our database on vegetated surfaces is extensive and includes surfaces such as forests, savannas, and croplands under a wide range of

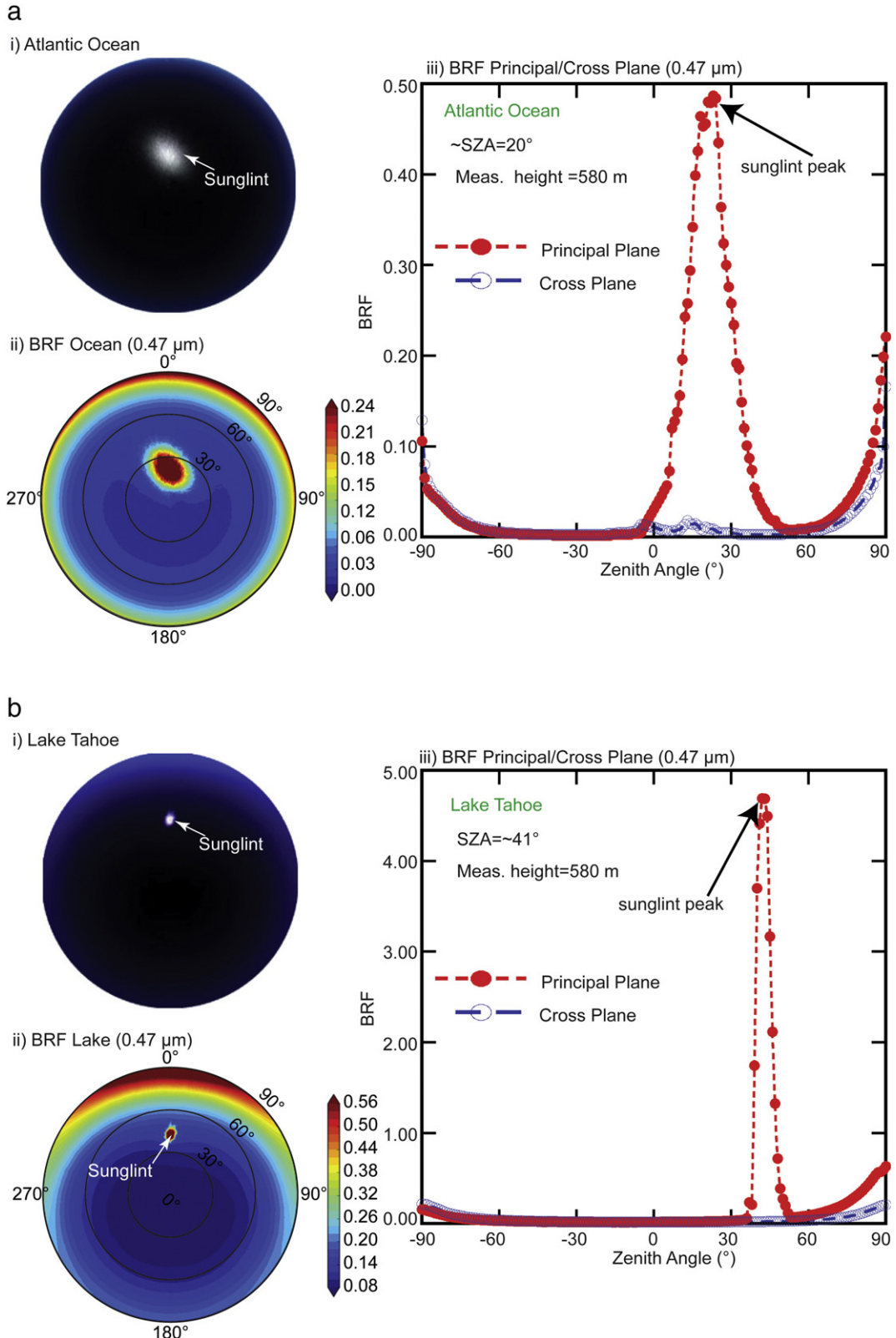


Fig. 5. a. (i.) CAR images of reflectance from the Atlantic ocean near Chesapeake Light, Virginia, constructed from bands at 1.04, 0.87, and 0.47 μm . (ii.) BRF of the Atlantic ocean at 0.47 μm , showing the dominant reflectance in the sunglint region. (iii.) BRF at 0.47 μm as a function of view zenith angle in the principal plane and cross plane. b. (i.) CAR images of reflectance from Lake Tahoe, a large freshwater lake in the Sierra Nevada, constructed from bands at 1.04, 0.87, and 0.47 μm . (ii.) BRF of Lake Tahoe at 0.47 μm , showing the dominant reflectance in the sunglint region. (iii.) BRF at 0.47 μm as a function of view zenith angle in the principal plane and cross plane.

solar zenith angles (cf. Fig. 6). For all of these surfaces, the BRDF or BRF pattern is primarily characterized by a hotspot. The “hotspot” is caused by the sensor observing the smallest proportion of shadows, resulting in

peak reflectance in the retro-reflection direction, where the sun is located directly behind the sensor. At the landscape scale, the BRDF pattern over trees is also influenced by the crown size, spacing between trees,

canopy density, canopy clumping, and the background soil BRDF. The arrangement of vegetation elements within the canopy and their orientation contributes to the anisotropy of reflectance, which enables information about the physical properties of the surface to be inferred. The

BRDF of these surfaces is also found to vary with time or season due to changes in vegetation phenology. The reflection function in the principal plane (and cross-perpendicular plane) shows a bowl or bell-shaped pattern.

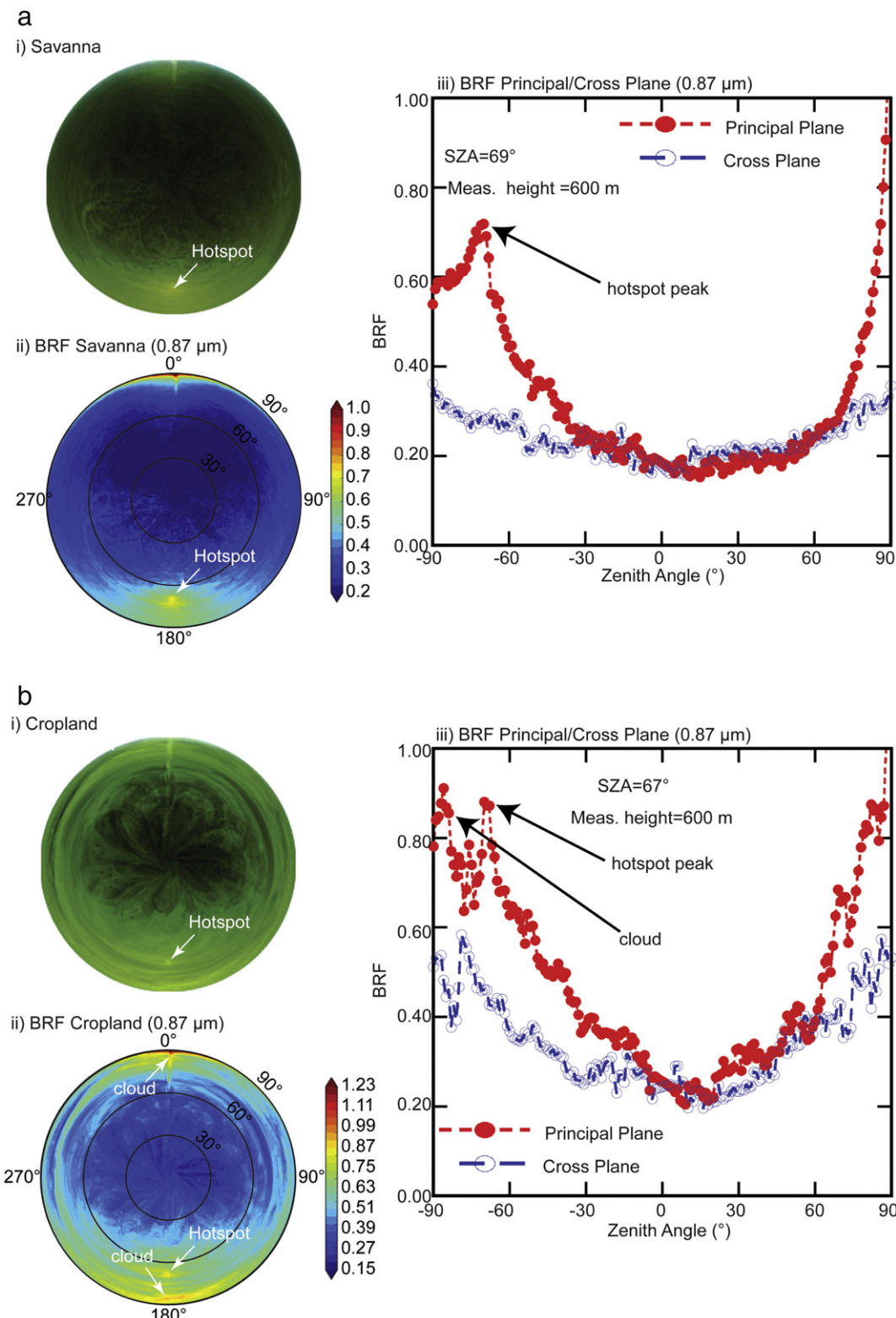


Fig. 6. a. (i.) CAR image of savanna (Skukuza, South Africa), constructed from bands at 1.04, 0.87, and 0.47 μm . (ii.) BRF at 0.87 μm shows a dominant hotspot in the backscattered (antisolar) direction. (iii.) BRF at 0.87 μm as a function of view zenith angle in the principal plane and cross plane. b. (i.) CAR image of croplands (Oklahoma), constructed from bands at 1.04, 0.87, and 0.47 μm . (ii.) BRF at 0.87 μm shows a dominant hotspot in the backscattered (antisolar) direction. (iii.) BRF at 0.87 μm as a function of view zenith angle in the principal plane and cross plane. c. (i.) CAR image of forests (Harvard Forest, Massachusetts), constructed from bands at 1.04, 0.87, and 0.47 μm . (ii.) BRF at 0.87 μm shows a dominant hotspot in the backscattered (antisolar) direction. (iii.) BRF at 0.87 μm as a function of view zenith angle in the principal plane and cross plane.

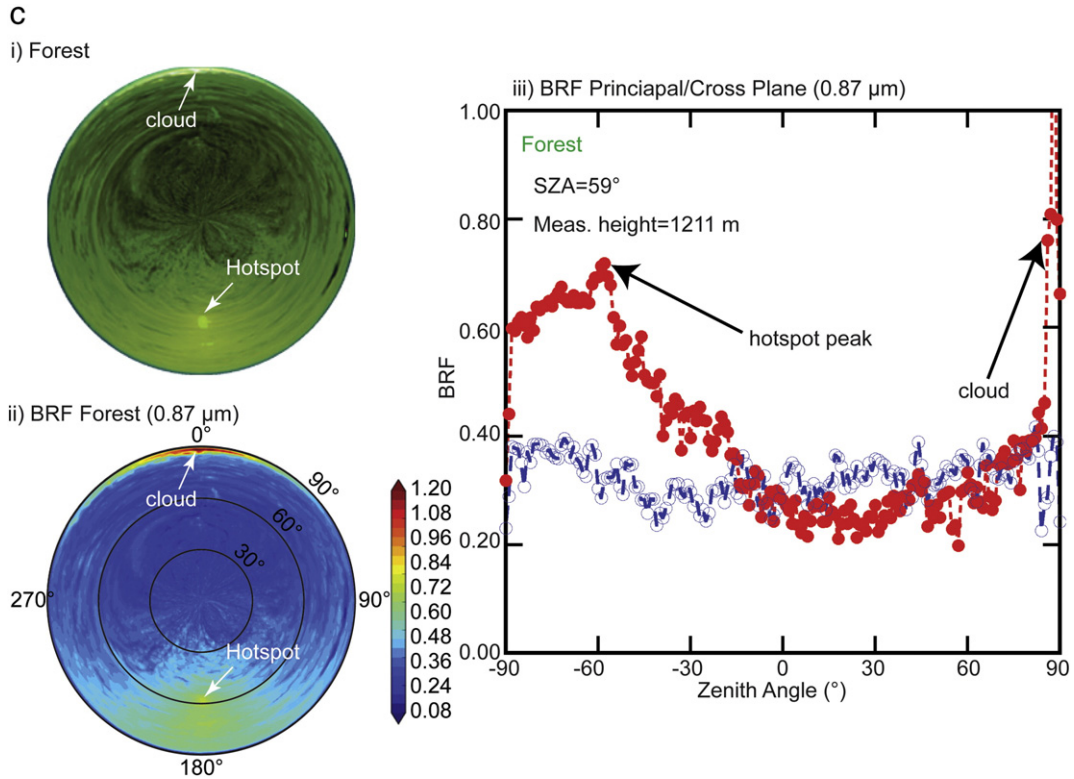


Fig. 6 (continued).

These BRDF datasets can be very useful in the validation of surface BRDF models for vegetated surfaces that require a combination of mathematical functions to quantify the intensity of reflectance and the pattern or shape of the BRDF (flat, bowl or bell), the strength of the anisotropy, the relative amount of forward and backward scattering, and a hotspot term. BRDF models are used to infer land surface parameters such as leaf area index (LAI), fraction of absorbed photosynthetically active radiation (FAPAR), aerodynamic surface roughness, net primary productivity, and albedo at different scales, which are needed for understanding the transfer of energy and mass transport between terrestrial ecosystems and the atmosphere (Roberts, 2001).

Fig. 6a(i) shows a multispectral image of CAR bands at 1.04, 0.87, and 0.47 μm for reflectance of savanna vegetation in Skukuza, South Africa on 29 August 2000, when $\theta_0 = 69^\circ$, **Fig. 6b(i)** shows a multispectral reflectance image of croplands near the Atmospheric Radiation Measurement (ARM) program Southern Great Plains (SGP) Cloud and Radiation Testbed (CART) site in Oklahoma on 24 June 2007, when $\theta_0 = 67^\circ$, and **Fig. 6c(i)** shows a multispectral image of reflectance of the Harvard Forest in Massachusetts on 19 September 2011, when $\theta_0 = 59^\circ$. In all of these cases the hotspot is readily apparent in the backscattering (antisolar) portion of these images. **Fig. 6(a–c)(ii)** & **(a–c)(iii)** show the BRF of each of these observations at 0.87 μm . Measurements such as these can be fit to analytical BRDF models often used in satellite remote sensing, such as the kernel-driven Rahman–Pinty–Verstraete (RPV) model (Rahman, Pinty, & Verstraete, 1993) used by MISR or the RossThick-LiSparse Reciprocal (RTLSR) model (Roujean, Leroy, & Deschamps, 1992) used by MODIS (Schaaf et al., 2002).

4.3. Clouds (liquid water and ice)

Variability of the angular reflectance pattern of clouds depends on the cloud optical properties (optical thickness, single scattering albedo, asymmetry factor) and microphysical properties (thermodynamic phase; water droplet or ice particle size distribution), as well as its 3-D structure. However, the anisotropy observed in the cloud BRDF or BRF

is primarily a function of its optical thickness and effective radius as well as its thermodynamic phase (liquid water or ice). For liquid water clouds, a decrease in effective radius makes the BRDF more isotropic at visible wavelengths, while more pronounced at near-infrared window wavelengths (Nakajima & King, 1990). The BRF is generally different for ice clouds as shown in **Fig. 7c**. Liquid water clouds have a unique pattern defined by single scattering features such as the cloudbow and glory, whereas ice clouds are characterized by a glint pattern in the forward scattering direction, which has a distinct peak in the solar direction whose magnitude and location in the principal plane depends on the solar zenith angle.

Our database includes cloud BRDF measurements over marine stratocumulus clouds off the Namibian and Californian coastlines, supercooled water clouds in Arctic Canada, ice clouds in Alaska, low cloud decks in the Gulf of Mexico near Veracruz, and the Atlantic Ocean off the US east coast near Chesapeake Bay.

Fig. 7a(i) shows a multispectral image of CAR bands at 1.04, 0.87, and 0.47 μm for reflectance of marine stratocumulus clouds composed of liquid water off the coast of California on 28 June 2008, when $\theta_0 = 27^\circ$, **Fig. 7b (i)** shows a multispectral image for reflectance of supercooled clouds near Norwegian Bay, Canada on 9 April 2008, when $\theta_0 = 71^\circ$, and **Fig. 7c (i)** shows a multispectral image for reflectance of an ice cloud near Fairbanks, Alaska on 13 April 2008, when $\theta_0 = 58^\circ$. **Fig. 7a(ii)–c(ii)** shows the BRF of each of these observations at 0.87 μm . The liquid water clouds show the presence of a cloudbow and glory due to the spherical cloud drops within these clouds, features that are lacking in the ice cloud, which shows no backscattering features but instead shows the presence of sunglint in the forward scattering direction as illustrated in the principal plane reflectances (**Fig. 7a(iii)–c(iii)**).

4.4. Snow and sea ice

Snow, ice, or both are key ingredients in every aspect of the cryosphere, including sea ice, glaciers, ice shelves, icebergs, and frozen

ground. The distinction between snow and ice lies in their formation. Snow is precipitation made up of ice crystals, which is formed when cold temperatures and high humidity levels combine in the atmosphere to form snow crystals. As long as the air temperature remains below

freezing, the crystals will fall to the Earth as snow. On the other hand, ice is formed when temperatures drop below the freezing point and liquid water becomes a solid, creating a tightly bonded substance. Sea ice is frozen ocean water, which is formed, grows, and melts in the ocean,

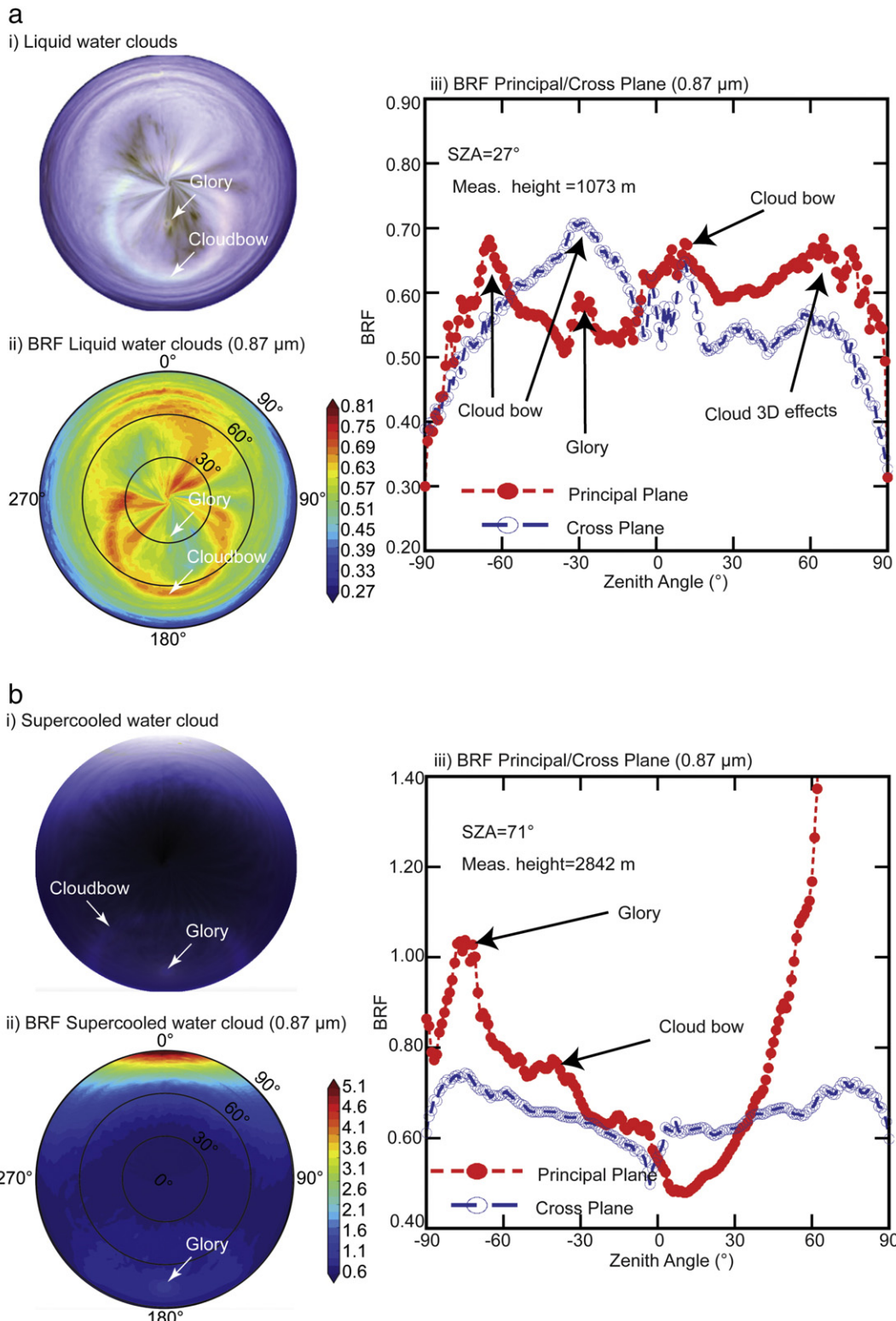


Fig. 7. a. (i.) CAR image of marine stratocumulus clouds (California) constructed from bands at 1.04, 0.87, and 0.47 μm . (ii.) BRF of liquid water clouds at 0.87 μm , showing the glory and cloudbow features. (iii.) BRF at 0.87 μm as a function of view zenith angle in the principal plane and cross plane. b. (i.) CAR image of supercooled water clouds (Norwegian Bay, Canada), constructed from bands at 1.04, 0.87, and 0.47 μm . (ii.) BRF of supercooled clouds at 0.87 μm , showing the glory and cloudbow features for liquid water clouds and sunglint. (iii.) BRF at 0.87 μm as a function of view zenith angle in the principal plane and cross plane. c. (i.) CAR image of ice clouds (Alaska), constructed from bands at 1.04, 0.87, and 0.47 μm . (ii.) BRF of ice clouds at 0.87 μm , showing the sunglint for ice clouds. (iii.) BRF at 0.87 μm as a function of view zenith angle in the principal plane and cross plane.

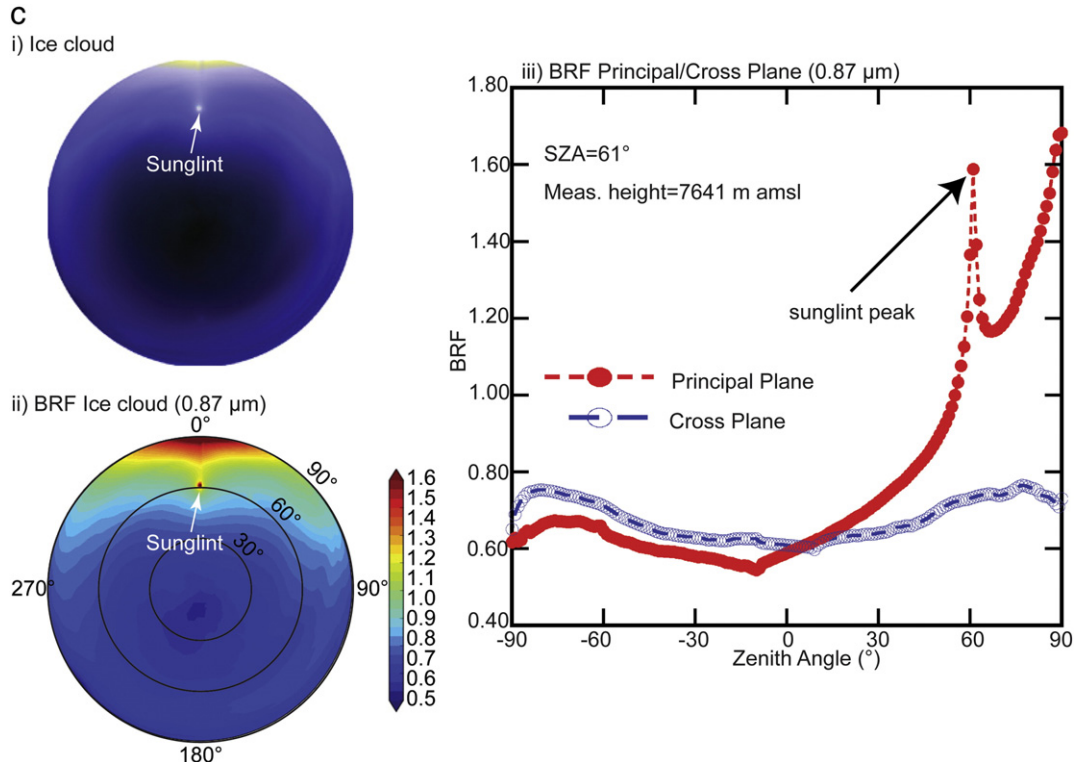


Fig. 7 (continued).

while icebergs, glaciers, and ice shelves float in the ocean but originate on land. For most of the year, sea ice is typically covered with snow, while the ice over land is built up from many seasons of snowfall. For our purpose we focus on sea ice, which forms an important aspect of both the Arctic region and Antarctica.

Ice and snow exist relatively close to their melting point and may frequently change from solid to liquid and back, resulting in dramatic visual changes across the landscape. According to Warren, Brandt, and Hinton (1998), surface roughness (on a scale larger than the wavelength of light) alters the angular pattern of sunlight reflected by snow due to changing grain size with age and wind induced features such as sastrugi, which cover vast areas of the polar region. For sea ice, BRDF or BRF anisotropy is characterized by brine and bubble concentrations, ice temperature, and ice thickness, coupled with the local meteorology (freeze-thaw cycles) (Perovich, Grenfell, Light, & Hobbs, 2002). Therefore, the BRF pattern of snow and sea ice is non-Lambertian and shows marked increases in the forward direction, especially for low solar elevation as shown in Fig. 8 (cf. Arnold et al., 2002; Warren et al., 1998).

Our database includes extensive snow/sea ice BRDF measurements over three common arctic surfaces: snow-covered sea ice, melt-season sea ice, and snow-covered tundra. These data were collected as part of the arctic Lead Experiment (LeadEx) in April 1992, the Arctic Radiation Measurements in Column Atmosphere-Surface System (ARMCAS) experiment in June 1995, and the Arctic Research of the Composition of the Troposphere from Aircraft and Satellites (ARCTAS) in April 2008. Note that during April the ice is covered by an optically thick layer of cold, dry snow, creating a bright, white, and uniform-appearing surface, while in June snow cover is usually melted and the surface is a mix of bare ice and some shallow ponds so that by August snow is completely melted and the surface is bare ice or melt ponds (Perovich, 2003).

Fig. 8a(i) shows a multispectral image of CAR bands at 1.04, 0.87, and 0.47 μm of reflectance of the snow-covered sea ice over Elson Lagoon, Barrow, Alaska on 6 April 2008, when $\theta_0 = 67^\circ$, and Fig. 8b(i) shows a

multispectral image for reflectance of sea ice in Nausen Sound, Ellesmere Island, Canada on 8 April 2008, when $\theta_0 = 73^\circ$. Fig. 8a(ii) and b(ii) shows the BRF of each of these observations at 0.87 μm , both of which exhibit nearly isotropic reflection except for enhancements in the forward reflectance direction at these low sun, Arctic, conditions. These features are clearly seen in the principal plane plots shown in Fig. 8a(iii) & b(iii).

4.5. Non-vegetated bright surfaces (dry lakebeds, desert)

Dry lakebeds and desert surfaces are generally defined by their lack of vegetation and are considered to be spatially uniform, spectrally stable over time, and near uniform (Lambertian) for small angles off nadir. Their sufficiently large spatial extent, low cloud cover, and low atmospheric aerosol loading make them suitable for vicarious calibration of satellite sensors.

Our database includes BRDF measurements over Railroad Valley Playa, Nevada, USA (May 2008), Etosha Pan, Namibia (September 2000), Sua Pan, Botswana (September 2000), and desert surfaces in Saudi Arabia (May 1991). The dry lakebed of Railroad Valley Playa is considered a desert site with no vegetation.

Fig. 9a(i) shows a multispectral image of CAR bands at 1.04, 0.87, and 0.47 μm of reflectance of Railroad Valley Playa, a dry lake bed in eastern Nevada, on 16 May 2008, when $\theta_0 = 23^\circ$, and Fig. 9b(i) shows a multispectral image of reflectance of the Saudi Arabian Desert on 28 May 1991, when $\theta_0 = 48^\circ$. Fig. 9a(ii) and b(ii) shows the corresponding BRF of each of these observations at 0.87 μm . The low altitude flight over Railroad Valley shows the shadow from the aircraft in the antisolar direction, but otherwise this nearly isotropic surface exhibits enhanced reflection in the backscattered direction relative to the forward scattering direction, similar in nature to that of Etosha Pan shown in Fig. 4c. The Saudi Arabian desert shown in Fig. 9b has nearly isotropic reflectance except for enhancements in the forward reflectance direction at $\theta > 50^\circ$.

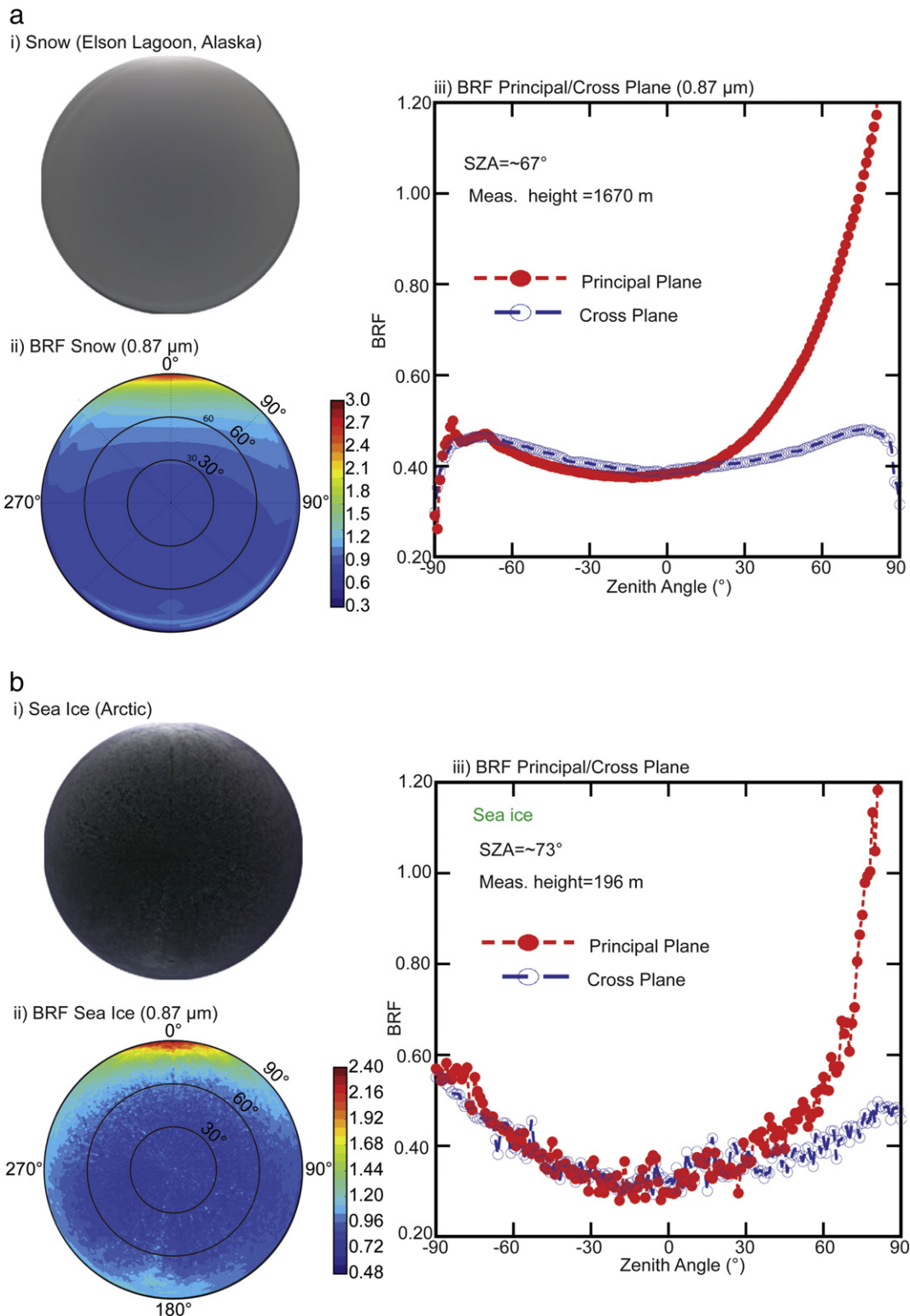


Fig. 8. a. (i.) CAR image of snow (Elson Lagoon, Alaska), constructed from bands at 1.21, 1.04, and 0.68 μm . (ii.) BRF of snow at 0.87 μm , showing near-Lambertian reflectance but with a prominent reflectance in the forward (specular) direction. (iii.) BRF at 0.87 μm as a function of view zenith angle in the principal plane and cross plane. b. (i.) CAR image of sea ice (Greenland), constructed from bands at 1.04, 0.87, and 0.47 μm . (ii.) BRF of sea ice at 0.87 μm , showing near-Lambertian reflectance but with a prominent reflectance in the forward (specular) direction. (iii.) BRF at 0.87 μm as a function of view zenith angle in the principal plane and cross plane.

4.6. Wetlands

Wetlands are complex hydrologic environments that are neither aquatic nor terrestrial and they are the largest source of atmospheric methane (CH_4) (Bubier, Rock, & Crill, 1997). The BRDF of wetlands is

determined by the percent of surface water (both turbid and clear) and percent of non-water (characterized by various vegetation types, including floating vegetation mats) in a scene. It is not unusual for the BRDF or BRF in this category to show both a glint in the forward scattering direction and a hotspot in the backscattering direction.

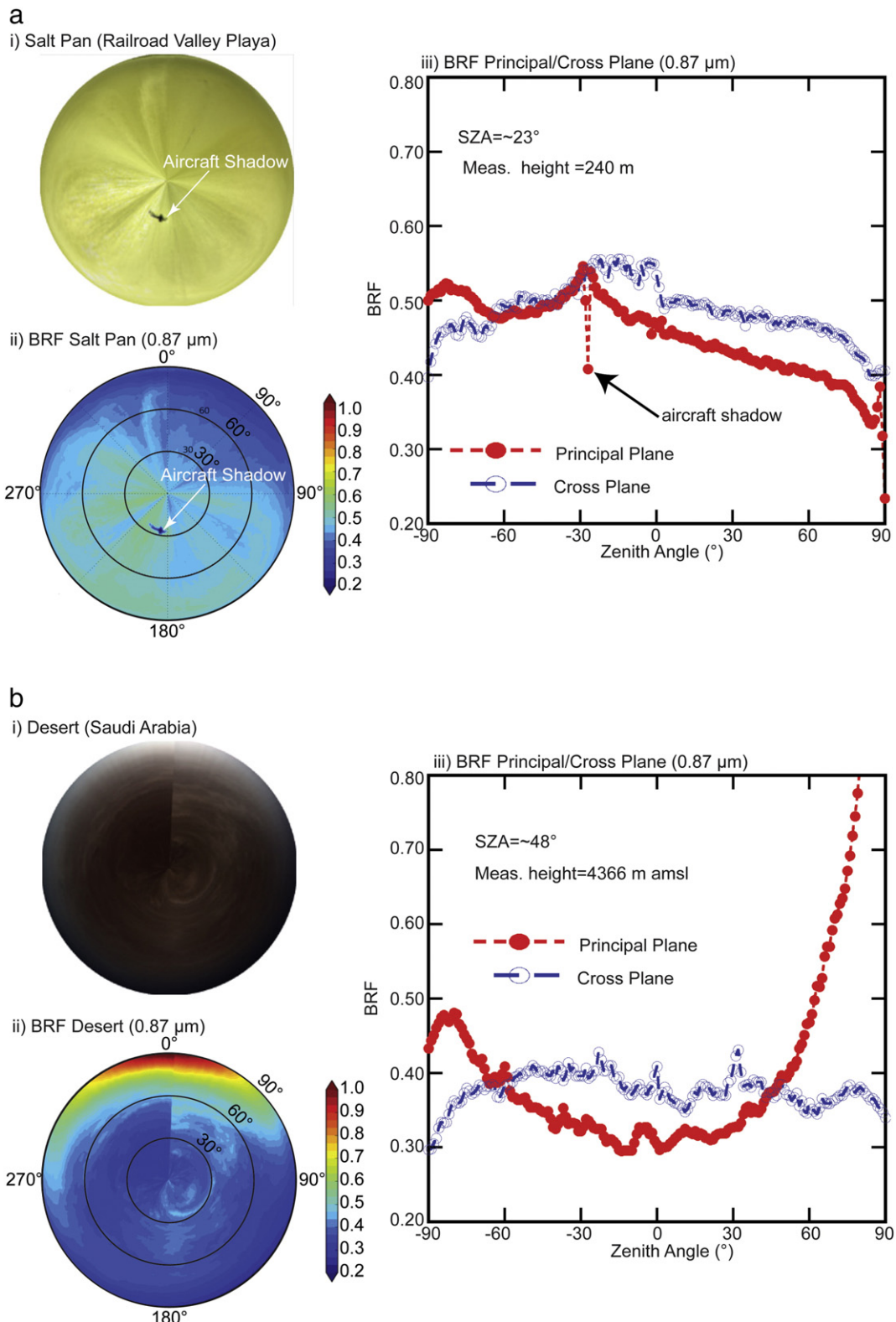


Fig. 9. a. (i.) CAR image of a bright, nonvegetated surfaces of a salt pan (Railroad Playa, Nevada, constructed from bands at 1.04, 0.87, and 0.67 μm). (ii.) BRF of salt pan at 0.87 μm with a hotspot feature appearing in the principal plane. (iii.) BRF at 0.87 μm as a function of view zenith angle in the principal plane and cross plane. b. (i.) CAR images of bright, nonvegetated surface of a desert (Saudi Arabia), constructed from bands at 1.04, 0.87, and 0.67 μm . (ii.) BRF of desert at 0.87 μm with enhanced reflectance in the forward direction. (iii.) BRF at 0.87 μm as a function of view zenith angle in the principal plane and cross plane.

Most of the CAR wetland datasets are scattered along coastal areas of the US. For example, along the US East coast, we have measurements over the Florida Coastal Everglades Long Term Ecological Research

(FCE LTER) station, Smithsonian Environmental Research Center (SERC), and the Great Dismal Swamp in the coastal plains of southeastern Virginia and northeastern North Carolina. Other wetland locations

where we have acquired BRDF measurements include the Elkhorn Slough National Estuarine Research Reserve in California, Fort McMurray along the Athabasca River in Alberta, Canada, northern Rondônia, Brazil, and Maputo, Mozambique.

Fig. 10a(i) shows a multispectral image of CAR bands at 1.04, 0.87, and 0.47 μm of reflectance of a mangrove forest in the Everglades National Park on 14 September 2011, when $\theta_0 = 64^\circ$, and **Fig. 10b(i)** shows a multispectral image of reflectance of the Great Dismal Swamp on 31 July

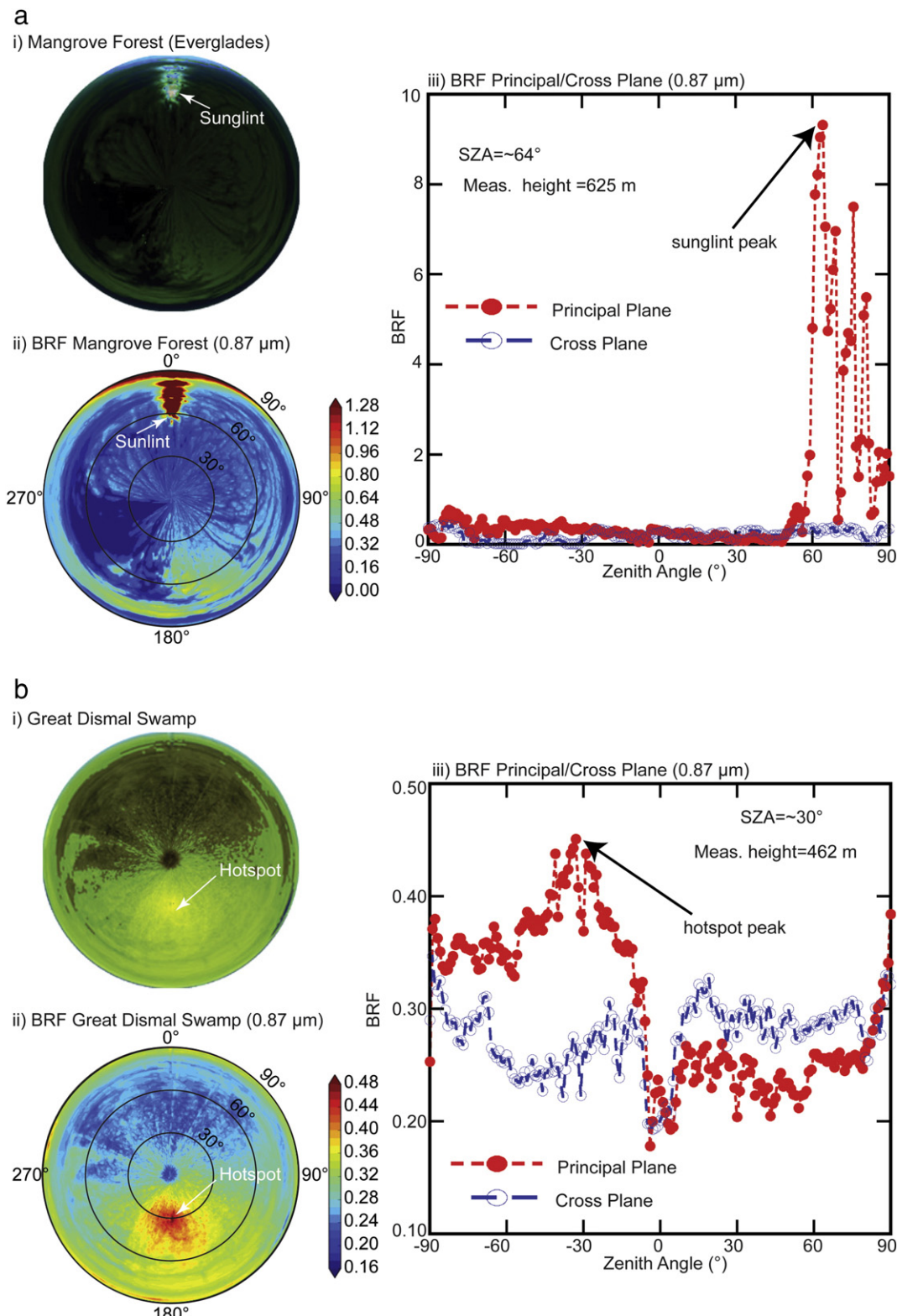


Fig. 10. a. (i.) CAR image of mangrove forest wetlands (Florida Everglades) constructed from bands at 1.04, 0.87, and 0.47 μm . (ii.) BRF of mangrove forest at 0.87 μm , showing enhanced sunglint reflectance in the forward direction. (iii.) BRF at 0.87 μm as a function of view zenith angle in the principal plane and cross plane. b. (i.) CAR image of the Great Dismal Swamp wetlands (southeastern Virginia), constructed from bands at 1.04, 0.87, and 0.47 μm . (ii.) BRF of the Great Dismal Swamp at 0.87 μm , showing a hotspot over the vegetated surfaces in the antisolar direction. (iii.) BRF at 0.87 μm as a function of view zenith angle in the principal plane and cross plane.

2001, when $\theta_0 = 48^\circ$. Fig. 10a(ii) and b(ii) shows the corresponding BRF of each of these observations at $0.87 \mu\text{m}$. Fig. 10a(ii) is unusual in that it clearly shows evidence of sunglint from the water in the Everglades

ecosystem as well as a hotspot in the backscattered direction associated with the mangrove forest. The Great Dismal Swamp shown in Fig. 10b(ii) has a very distinctive hotspot in the backscattering, antisolar

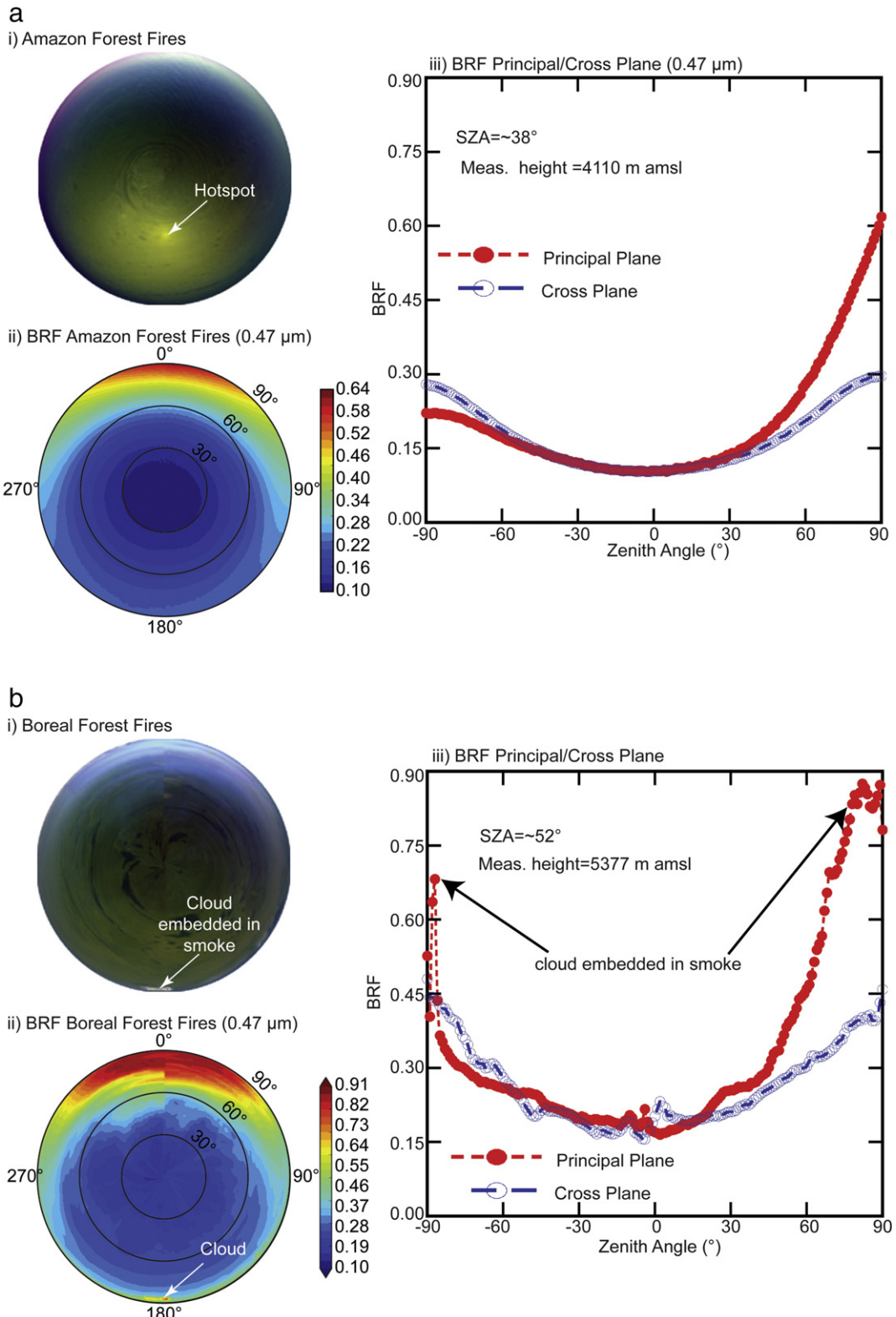


Fig. 11. a. (i.) CAR image of smoke from Amazon forest fires (Brazil), constructed from bands at $1.04, 0.87$, and $0.47 \mu\text{m}$. (ii.) BRF of Amazon smoke at $0.47 \mu\text{m}$, a wavelength that is opaque to the surface but shows prominent scattering from the smoke layer. (iii.) BRF at $0.47 \mu\text{m}$ as a function of view zenith angle in the principal plane and cross plane. b. (i.) CAR image of smoke of Boreal forest fires (Saskatchewan, Canada), constructed from bands at $1.04, 0.87$, and $0.47 \mu\text{m}$. (ii.) BRF of Boreal smoke at $0.47 \mu\text{m}$, a wavelength that is opaque to the surface but shows prominent scattering from the smoke layer. The presence of clouds embedded in the smoke shows enhanced reflectance. (iii.) BRF at $0.47 \mu\text{m}$ as a function of view zenith angle in the principal plane and cross plane.

direction. This ecosystem has a thicker canopy of trees overlying the waterways and thus primarily shows the vegetation hotspot to be expected from dense dark vegetation. In both cases the cross sections through the principal and cross plane are shown in Fig. 10a(iii) and b(iii).

4.7. Smoke (biomass and oil)

The angular reflectance distribution of an optically thick smoke layer, where the ground is invisible in the UV-visible spectral region, shows fairly smooth and symmetric patterns. Smoke is extremely variable in composition and size distribution—smoke being a complex mixture of many chemicals including carbon dioxide, water vapor, carbon monoxide, particles, hydrocarbons, nitrogen oxides, and thousands of other compounds. The actual composition of smoke depends on the type of fuel (wood, vegetation, oil, etc.) being burnt, the temperature of the fire, and the wind conditions. Particles from smoke tend to be very small – less than one micrometer in diameter.

These unique smoke BRDF data were obtained during the Kuwait oil fire, ARCTAS, SAFARI-2000, and SCAR-B campaigns. These data enable construction of observationally constrained angular directional models (ADMs) that are needed for computing fluxes at the top of the atmosphere (TOA) for spaceborne radiation instruments, such as the Clouds and the Earth's Radiant Energy System (CERES) described by Wielicki et al. (1996).

Fig. 11a(i) shows a multispectral image of CAR bands at 1.04, 0.87, and 0.47 μm of reflectance of an Amazon forest fire near Porto Velho, Brazil on 6 September 1995, when $\theta_0 = 38^\circ$, and Fig. 11b(i) shows a multispectral image of reflectance of a boreal forest fire in northern Saskatchewan, Canada on 30 June 2008, when $\theta_0 = 52^\circ$. Fig. 11a(ii) and b(ii) shows the corresponding BRF of both of these observations at 0.47 μm , a wavelength for which the ground surface is clearly obscured by the multiple scattering of the smoke, which yields a very smooth reflectance pattern. Both exhibit a smooth forward scattering pattern and a bowl-like scattering pattern as shown in the principal and cross plane (Fig. 10a(iii) & b(iii)). Fig. 11b(iii) shows enhancement in both the forward and backscattering directions due to the presence of a small cloud embedded in the smoke. The Amazonas case in Fig. 11a(iii) is especially optically thick such that the reflectance pattern is quite symmetric with a well-defined cross-plane reflectance pattern.

5. Summary and conclusions

The Cloud Absorption Radiometer (CAR), originally designed for making scattered solar radiation measurements deep within a cloud layer over a wide angular range (190°) for determining the spectral absorption of solar radiation by clouds, has been used most extensively since 1991 for measuring the bidirectional reflectance-distribution function of a wide variety of terrestrial surfaces as well as clouds and smoke embedded in the atmosphere. This has been accomplished due to its unique design with its small field of view, large scanning angle, and integration on a wide variety of aircraft from the University of Washington (B-23, C-131A, CV-580), South African Weather Service (AeroCommander 690A), Sky Research (Jetstream J-31), and NASA (P-3B).

Our BRDF database encompasses various natural surfaces that are representative of many land cover or ecosystem types found throughout the world. CAR's unique measurement geometry allows a comparison of measurements acquired from different satellite instruments with various geometrical configurations, none of which are capable of obtaining such a complete and nearly instantaneous BRDF. This database is therefore of great value in validating many satellite sensors and assessing corrections of reflectances for angular effects. These data can be used to evaluate the ability of analytical models to reproduce the observed directional signatures and to develop BRDF models that are suitable for sub-kilometer-scale satellite observations over both

homogeneous and heterogeneous landscape types. All of these BRDF data, which include multiple wavelengths in the visible and near-infrared, are publicly available and accessible in hierarchical data format from <http://car.gsfc.nasa.gov/data/>.

Acknowledgments

The authors are especially grateful to Rajesh Poudyal, G. Thomas Arnold, Jason Y. Li, and Howard G. Meyer for data processing, and Manoj Kumar for support with some of the figures. This research is supported by the Science Mission Directorate of the National Aeronautics and Space Administration under the Radiation Sciences program managed by Hal Maring.

References

- Abdou, W. A., Pilorz, S. H., Helmlinger, M. C., Conel, J. E., Diner, D. J., Bruegge, C. J., et al. (2006). *Sua Pan surface bidirectional reflectance: A case study to evaluate the effect of atmospheric correction on the surface products of the Multi-angle Imaging SpectroRadiometer (MISR) during SAFARI 2000*. *IEEE Transactions on Geosciences and Remote Sensing*, 44, 1699–1706.
- Arnold, G. T., King, M. D., Tsay, S. C., Li, J. Y., & Soulen, P. F. (2002). Airborne spectral measurements of surface-atmosphere anisotropy for Arctic sea ice and tundra. *International Journal of Remote Sensing*, 23, 3763–3781.
- Barnsley, M. J., Settle, J. J., Cutler, M. A., Lobb, D. R., & Teston, F. (2004). The PROBA/CHRIS mission: A low-cost smallsat for hyperspectral, multiangle, observations of the Earth surface and atmosphere. *IEEE Transactions on Geoscience and Remote Sensing*, 42, 1512–1520.
- Bubier, J. L., Rock, B. N., & Crill, P. M. (1997). Spectral reflectance measurements of boreal wetland and forest mosses. *Journal of Geophysical Research*, 102, 29483–29494.
- Cox, C., & Munk, W. (1954a). The measurements of the roughness of the sea surface from photographs of the sun's glitter. *Journal of the Optical Society of America*, 4, 838–850.
- Cox, C., & Munk, W. (1954b). Statistics of the sea surface derived from sun glitter. *Journal of Marine Research*, 13, 198–227.
- Deschamps, P. Y., Bréon, F. M., Leroy, M., Podaire, A., Bricaud, A., Buriez, J. C., et al. (1994). The POLDER mission: Instrument characteristics and scientific objectives. *IEEE Transactions on Geoscience and Remote Sensing*, 32, 598–615.
- Diner, D. J., Asner, G., Davies, R., Knyazikhin, Y., Müller, J. P., Nolin, A. W., ... Stroeve, J. (1999). New directions in Earth observing: Scientific applications of multiangle remote sensing. *Bulletin of the American Meteorological Society*, 80, 2209–2228.
- Diner, D. J., Beckert, J. C., Reilly, T. H., Bruegge, C. J., Conel, J. E., Kahn, R., Martonchik, J. V., et al. (1998). Multiangle Imaging SpectroRadiometer (MISR) description and experiment overview. *IEEE Transactions on Geoscience and Remote Sensing*, 36, 1072–1087.
- Diner, D. J., Braswell, B. H., Davies, R., Gobron, N., Hu, J., Kahn, R. A., ... Stroeve, J. (2005). The value of multiangle measurements for retrieving structurally and radiatively consistent properties of clouds, aerosols, and surfaces. *Remote Sensing of Environment*, 97, 495–518.
- Diner, D. J., Di Girolamo, L., & Nolin, A. W. (2007). Multi-angle Imaging SpectroRadiometer – Special Issue. *Remote Sensing of Environment*, 107, 1–384.
- Doxaran, D., Nagur-Cherukuru, R. C., & Lavender, S. J. (2004). Estimation of surface reflection effects on upwelling radiance field measurements in turbid waters. *Journal of Optics A: Pure and Applied Optics*, 6, 690–697.
- Gatebe, C. K., Butler, J. J., Cooper, J. W., Kowalewski, M., & King, M. D. (2007). Characterization of errors in the use of integrating-sphere systems in the calibration of scanning radiometers. *Applied Optics*, 46, 7640–7651.
- Gatebe, C. K., Dubovik, O., King, M. D., & Sinyuk, A. (2010). Simultaneous retrieval of aerosol and surface optical properties from combined airborne- and ground-based direct and diffuse radiometric measurements. *Atmospheric Chemistry and Physics*, 10, 2777–2794.
- Gatebe, C. K., King, M. D., Lyapustin, A. I., Arnold, G. T., & Redemann, J. (2005). Airborne spectral measurements of ocean directional reflectance. *Journal of the Atmospheric Sciences*, 62, 1072–1092.
- Gatebe, C. K., King, M. D., Platnick, S., Arnold, G. T., Vermote, E. F., & Schmid, B. (2003). Airborne spectral measurements of surface-atmosphere anisotropy for several surfaces and ecosystems over southern Africa. *Journal of Geophysical Research*, 108, 8489. <http://dx.doi.org/10.1029/2002JD002397>.
- Gatebe, C. K., Varnai, T., Poudyal, R., Ichoku, C., & King, M. D. (2012). Taking the pulse of pyrocumulus clouds. *Atmospheric Environment*, 52, 121–130.
- Gatebe, C. K., Wilcox, E., Poudyal, R., & Wang, J. (2011). Effects of ship wakes on ocean brightness and radiative forcing over ocean. *Geophysical Research Letters*, 38, L17702. <http://dx.doi.org/10.1029/2011GL048819>.
- Georgiev, G. T., Gatebe, C. K., Butler, J. J., & King, M. D. (2009). BRDF analysis of savanna vegetation and salt-pan samples. *IEEE Transactions on Geoscience and Remote Sensing*, 47, 2546–2556.
- Hapke, B. (1981). Bidirectional Reflectance Spectroscopy: 1. Theory. *Journal of Geophysical Research*, 86, 3039–3054.
- Hautecoeur, O., & Leroy, M. (1998). Surface bidirectional reflectance distribution function observed at global scale by POLDER/ADEOS. *Geophysical Research Letters*, 25, 4197–4200.
- Kahle, D., Gatebe, C. K., McCune, B., & Dustan, H. (2013). Cloud Absorption Radiometer Navigation System (CANS). *NASA Technical Reports Server (NTRS)* (Document ID: 20130013813). <http://ntrs.nasa.gov/search.jsp?R=20130013813>.

- King, M. D. (1992). Directional and spectral reflectance of the Kuwait oil-fire smoke. *Journal of Geophysical Research*, 97, 14545–14549.
- King, M. D., Radke, L. F., & Hobbs, P. V. (1990). Determination of the spectral absorption of solar radiation by marine stratocumulus clouds from airborne measurements within clouds. *Journal of the Atmospheric Sciences*, 47, 894–907.
- King, M. D., Strange, M. G., Leone, P., & Blaine, L. R. (1986). Multiwavelength scanning radiometer for airborne measurements of scattered radiation within clouds. *Journal of Atmospheric and Oceanic Technology*, 3, 513–522.
- Koukal, K., & Atzberger, C. (2012). Potential of multi-angular data derived from a digital aerial frame camera for forest classification. *IEEE Journal of Selected Topics in Applied Earth Observations and Remote Sensing*, 5, 30–43.
- Lenoble, J. (1993). *Atmospheric radiation transfer*. A. Hampton, Virginia, USA: Deepak Pub (532 pp.).
- Liang, S., & Strahler, A. (Eds.). (2000). *Land surface bidirectional reflectance distribution function (BRDF): Recent advances and future prospects*. *Remote Sensing Reviews*, 18. (pp. 83–551).
- Lin, Z., Li, W., Gatebe, C. K., Poudyal, R., & Starnes, K. (2016). Radiative transfer simulations of the two-dimensional ocean glint reflectance and determination of the sea surface roughness. *Applied Optics*, 55, 1206–1215. <http://dx.doi.org/10.1364/AO.55.001206>.
- Longbotham, N., Chaapel, C., Bleiler, L., Padwick, C., Emery, W. J., & Pacifica, F. (2012). Very high resolution multiangle urban classification analysis. *IEEE Transactions on Geoscience and Remote Sensing*, 50, 1155–1170.
- Lyapustin, A., Gatebe, C. K., Kahn, R., Brandt, R., Redemann, J., Russell, P., King, M. D., et al. (2010). Analysis of snow BRDF from ARCTAS Spring-2008 campaign. *Atmospheric Chemistry and Physics*, 10, 4359–4375.
- Martonchik, J. V., Bruegge, C. J., & Strahler, A. (2000). A review of reflectance nomenclature used in remote sensing. *Remote Sensing Reviews*, 19, 9–20.
- McCamy, C. S. (2001). Concepts, terminology, and notation for optical modulation. In David R. Lide (Ed.), *Measurements, standards, and technology*. National Institute of Standards and Technology, Spec. Publ., 958. . Washington, DC: CRC Press (395 pp.).
- Nag, S., Gatebe, C. K., & Weck, O. L. (2015). Observing system simulations for small satellite clusters estimating bidirectional reflectance. *International Journal of Applied Earth Observation and Geoinformation*, 43, 102–118.
- Nakajima, T., & King, M. D. (1990). Determination of optical thickness and effective particle radius of clouds from reflected solar radiation measurements. Part I: Theory. *Journal of the Atmospheric Sciences*, 47, 1878–1893.
- Nicodemus, F. E. (1970). Reflectance nomenclature and directional reflectance and emissivity. *Applied Optics*, 9, 1474–1475.
- Nicodemus, F. E., Richmond, J. C., Hsia, J. J., Ginsberg, I. W., & Limperis, T. (1977). Geometric considerations and nomenclature for reflectance. U.S.A. Department of Commerce/National Bureau of Standards. *NBS Monograph*, 160 (52 pp.).
- Perovich, D. K. (2003). Complex yet translucent: The optical properties of sea ice. *Physica B*, 338, 107–114.
- Perovich, D. K., Grenfell, T. C., Light, B., & Hobbs, P. V. (2002). Seasonal evolution of the albedo of multiyear Arctic sea ice. *Journal of Geophysical Research*, 107, 8044. <http://dx.doi.org/10.1029/2000JC000438>.
- Rahman, H., Pinty, B., & Verstraete, M. M. (1993). Coupled surface-atmosphere reflectance (CSAR) model 2. Semiempirical surface model usable with NOAA advanced very high resolution radiometer data. *Journal of Geophysical Research*, 98(20), 791–20,801.
- Rees, W. G. (1990). *Physical principles of remote sensing*. Cambridge, UK: Cambridge University Press (247 pp.).
- Roberts, G. (2001). A review of the application of BRDF models to infer land cover parameters at regional and global scales. *Progress in Physical Geography*, 25, 483–511. <http://dx.doi.org/10.1177/03091330102500402>.
- Román, M. O., Gatebe, C. K., Poudyal, R., Schaaf, C. B., Wang, Z., & King, M. D. (2011). Variability in surface BRDF at different spatial scales (30 m–500 m) over a mixed agricultural landscape as retrieved from airborne and satellite spectral measurements. *Remote Sensing of Environment*, 115, 2184–2203.
- Roujean, J., Leroy, M., & Deschamps, P. (1992). A bidirectional reflectance model of the Earth's surface for the correction of remote sensing data. *Journal of Geophysical Research*, 97, 20,455–20,468.
- Schaaf, C. B., Gao, F., Strahler, A. H., Lucht, W., Li, X., Tsang, T., Strugnell, N. C., et al. (2002). First operational BRDF, albedo and nadir reflectance products from MODIS. *Remote Sensing of Environment*, 83, 135–148.
- Schaepman-Strub, G., Schaepman, M. E., Painter, T. H., Dangel, S., & Martonchik, J. V. (2006). Reflectance quantities in optical remote sensing—definitions and case studies. *Remote Sensing of Environment*, 103, 27–42.
- Soulen, P. F., King, M. D., Tsay, S. C., Arnold, G. T., & Li, J. Y. (2000). Airborne spectral measurements of surface-atmosphere anisotropy during the SCAR-A, Kuwait oil fire, and TARFOX experiments. *Journal of Geophysical Research*, 105, 10203–10218.
- Tanré, D., Bréon, F. M., Deuzé, J. L., Dubovik, O., Ducos, F., François, P., ... Waquet, F. (2011). Remote sensing of aerosols by using polarized, directional and spectral measurements within the A-Train: the PARASOL mission. *Atmospheric Measurement Techniques*, 4, 1383–1395.
- Torrance, K. E., & Sparrow, E. M. (1967). Theory for off-specular reflection from roughened surfaces. *Journal of the Optical Society of America*, 57, 1105–1114.
- Tsay, S. C., King, M. D., Arnold, G. T., & Li, J. Y. (1998). Airborne spectral measurements of surface anisotropy during SCAR-B. *Journal of Geophysical Research*, 103, 31943–31954.
- Vermote, E. F., Tanré, D., Deuzé, J. L., Herman, M., & Morcrette, J. J. (1997). Second simulation of the satellite signal in the solar spectrum, 6S: An overview. *IEEE Transactions on Geoscience and Remote Sensing*, 35, 675–686.
- Warren, S. G., Brandt, R. E., & Hinton, P. O'. R. (1998). Effect of surface roughness on bidirectional reflectance of Antarctic snow. *Journal of Geophysical Research*, 103, 25789–25807.
- Wielicki, B. A., Barkstrom, B. R., Harrison, E. F., Lee, R. B., III, Smith, G. L., & Cooper, J. E. (1996). Clouds and the Earth's Radiant Energy System (CERES): An earth observing system experiment. *Bulletin of the American Meteorological Society*, 77, 853–868.